A SURVEY OF THERMAL INSTABILITIES IN TOKAMAK PLASMAS: THEORY, COMPARISON WITH EXPERIMENT, AND PREDICTIONS FOR FUTURE DEVICES

W. M. STACEY *Georgia Institute of Technology*
Fusion Research Center, Atlanta, Georgia 30332-0425

Received January 6, 2006
Accepted for Publication September 20, 2006

The strong temperature dependence, over certain temperature ranges, of the radiation cooling rate of low-Z impurities, of the atomic physics cooling and particle source rates associated with recycling and fueling neutrals, of the ion-electron recombination particle loss rate, of the turbulent transport loss rate, and of the fusion alpha-particle heating rate have all been identified as "drivers" of thermal instabilities in the coupled plasma particle, momentum, and energy balances. This paper surveys the experimental observations of a number of abrupt transition phenomena in plasma operating conditions—i.e., density-limit disruptions, multifaceted asymmetric radiations from the edge (MARFEs), divertor MARFEs, detachment, in-out divertor heat flux asymmetries, H-L and L-H transitions, confinement, and pedestal deterioration—or anticipated in future reactors—i.e., power excursions—their theoretical interpretations in terms of thermal instabilities driven by the temperature dependence of various radiative and atomic physics cooling mechanisms, and a comparison of theoretical prediction with experimental observations. Also surveyed are theoretical predictions of thermal instabilities in the power balance driven by the strong positive temperature dependence of the fusion heating rate.

KEYWORDS: *thermal instabilities, radiative instabilities, density limits*

I. INTRODUCTION

Thermal instabilities have been identified as the probable cause of many abrupt-transition phenomena observed in tokamak experiments over the years, and the elements of a theoretical framework for thermal instability analysis have evolved in response to the challenge of understanding these phenomena. The first study of a thermal instability was stimulated solely by a theoretical insight, however, when in 1969 Mills[1] pointed out the destabilizing nature that the strong temperature dependence of the D-T fusion rate $\langle \sigma v \rangle \sim T^2$ would have on the thermal balance of a D-T plasma. A year later, Furth et al.[2] undertook an explanation of the observed contraction of the current channel leading to the radial collapse of the temperature profile followed by a disruption as a radiative thermal instability of the ohmic-heated temperature profile. These papers were the first of many that have since appeared concerned with instabilities in the energy and particle balances driven by the temperature dependence of the fusion or other heating rate or driven by the temperature dependence of the impurity radiative cooling rate. It was realized at a quite early stage that the temperature dependence of the plasma cooling rate arising from other atomic physics processes (charge exchange, ionization, and recombination) involving recycling neutrals could also cause similar thermal instabilities. Subsequently, it was realized that the temperature dependence of the transport energy loss rate could drive or stabilize thermal instabilities.

For our purposes here, we identify "thermal instabilities" as those instabilities in the particle and power balances driven primarily by the unfavorable temperature (and density) dependence of the plasma heating and cooling rates. Electromagnetic forces may also be involved, but the focus of this paper is on instabilities in the power and particle balances, the experimental manifestations of these instabilities, the theory that has been developed to describe them, and a comparison of this theory with experimental data.

The main purpose in preparing this survey is to take the first step in the codification and unification of this body of thermal instability research by collecting the

*E-mail: weston.stacey@nre.gatech.edu

various theoretical and computational analyses of thermal instabilities and the related experimental observations within a common framework, thereby exposing a commonality among the causes of several seemingly disparate phenomena. A second purpose is to identify the underlying parameters on which the onset of these instability phenomena depend. The survey encompasses a number of actively investigated phenomena with different experimental manifestations—radiative collapse leading to disruption, multifaceted asymmetric radiations from the edge (MARFEs), detachment and divertor MARFEs, divertor heat flux asymmetries, the low-to-high (L-H)–mode confinement transition, deterioration of confinement, and density limits—all of which are believed to have a common cause in thermal instabilities driven by impurity radiation or recycling neutral or turbulent transport cooling of the plasma. Also included is the theoretically predicted instability of a D-T plasma associated with the $\langle \sigma v \rangle \sim T^2$ dependence of the fusion heating rate. Not included are primarily electromagnetic instabilities nor the edge-localized modes (ELMs) that, while clearly involving a magnetohydrodynamic (MHD) instability, may have a (yet unelucidated) thermal instability trigger.

The survey is organized along historical lines. The first part deals with instabilities that have been primarily associated with impurity and atomic physics radiative cooling, and the second part deals with instabilities that have been primarily associated with fusion heating. This separation is somewhat arbitrary—e.g., radiative and transport cooling are important factors in fusion heating instabilities, and plasma heating is an important factor in radiative cooling instabilities—but has the advantage of being familiar, which should make the survey more accessible. Within the radiative cooling instabilities category, where the history has been first observation of an abrupt transition phenomenon followed by a theoretical explanation in terms of a thermal instability, the organization is by observable phenomena. Within the fusion plasma heating category, where the original insight was and still is theoretical, and the work has centered on theoretical methods of analysis and control, the organization is in terms of those methods. As the field moves forward into broader theoretical studies and later into experimental studies of burning plasmas, it is likely that new or modified thermal instabilities will be discovered that encompass elements of both the radiative cooling and the plasma heating instabilities discussed in this survey. Hopefully, this survey of the two related topics will provide a useful reference for such future work.

The general approach followed for the most part in this survey is first to characterize the experimental manifestation of the particular thermal instability (e.g., MARFEs) sufficiently to establish what evidence the thermal instability theory must explain, then to summarize the lines of development of the theoretical explanations, and finally to summarize the existing qualitative and quantitative comparisons of theoretical prediction and experimental observation. The choice of experimental work to include is selective—as required to characterize the instability or recognize seminal work—rather than comprehensive. The choice of equations to include is also selective, intended either to illustrate the lines of development and the nature of the recent results that represent the present state of the art or to recognize seminal work.

II. COLLAPSE OF TEMPERATURE PROFILE

II.A. Disruptions

Interest in the radiative collapse of the temperature profile in tokamaks was first stimulated by the observation that disruptions are frequently preceded by a radiative collapse of the temperature profile and an attendant shrinking of the current channel, followed by an MHD tearing mode leading to loss of confinement and plasma current. Since their discovery,[3] disruptions have been found to be ubiquitous in tokamaks. The experimental features were studied extensively by Sauthoff et al.[4] and in subsequent work. An informative experimental anatomy of disruptions in the Joint European Torus (JET) was assembled by Wesson et al.[5]

II.B. Radiative Collapse

The connection between the radial collapse of the temperature profile and disruptions led several researchers[6–11] to examine the thermal instability of the temperature profile produced by a central heating source and a radiative cooling loss due to a band of partially ionized impurity ions in the edge plasma. Gibson[6] demonstrated the importance of impurity radiation in the edge region in initiating the sequence of processes leading to what has become known as a "density limit disruption." Ohyabu[7] demonstrated by balancing a conductive heat source against radiative loss that a band of radiating impurities at the edge would cause the temperature profile to become unstable if the edge density is greater than a critical value $n_c(a) \sim < \{f_z^{-1}[T(0)/T(a)][\kappa_\perp/(-dL_z/dT)]\}^{1/2}$, where 0 and a refer to the center and the edge of the plasma, f_z is the impurity concentration in the edge, $\kappa_\perp$ is the thermal diffusivity, and L_z is the impurity radiative emissivity. Ashby and Hughes[8] considered the same problem and found a critical edge impurity concentration for radial temperature profile collapse, which can be rearranged to obtain a critical edge density $n_c(a) \sim \{(9/2)f_z^{-1}(\kappa_\perp/L_z)[T_{av}^2/T(a)]\}^{1/2}$ above which the temperature profile becomes unstable to radial collapse. Perkins and Hulse[9] balanced core heating against edge radiation and found a critical value of the core density $n_{cav} \sim (B/R)/(Z_{eff}-1)^{1/2}$, above which the radial temperature profile was unstable. Stacey[10,11] examined the same problem and found critical

edge densities $n_c(a) \sim \{f_z^{-1}(1/L_z)[T(0)/T(a)]\}^{1/2}$ and $n_c(a) \sim \{f_z^{-1}[\chi_\perp/(-dL_z/dT)]\}/a^2$, where $n(a)\chi_\perp = \kappa_\perp$. Mahdavi et al.[12] found a stability condition $1 + 2\ln(r_{mant}/a_{plasma})(1 + H/L_z) \geq 0$ for the inner radius of a radiating mantle in terms of the core heating (H) and mantle radiative cooling (L_z) rates.

The most detailed analysis to date of the radiative collapse of the temperature profile is that of Stacey,[11] who considered the stability of coupled radial temperature and density transport equations against perturbations of the form $T(r,t) = \bar{T}(r) + \tilde{T}(r)e^{\omega t}$ and a similar expression for the density perturbations. Considering first only an instability in the temperature profile, it was found that the temperature perturbation satisfied a form Bessel's equation for $J_0(\mu r/a)$ when a certain composite term was replaced by a spatial average value of the heating and cooling terms weighted by $\tilde{T}(r)$, which term was designated $\kappa_\perp \mu^2$. Since the radiation is localized in the outer region, the temperature collapse would start in the outer region and move progressively inward. This sort of temperature perturbation was approximately represented by $\tilde{T}(r) \approx J_0(\mu r/a)$ with the second zero crossing ($\mu = 5.5$) at the boundary ($r = a$), which is negative in the outer region ($2.4 < \mu r/a < 5.5$). Solving the dispersion relation for the growth rate and setting this quantity to zero then led to an expression for the maximum density for which the plasma is stable against collapse of the radial temperature distribution:

$$n \leq \frac{\chi_\perp(5.5/a)^2\left[1 \pm \left\{\sqrt{1 + 4\langle -\partial\hat{H}/\partial T\rangle\langle \tfrac{1}{4}U_\alpha[\partial(\sigma v)/\partial T] + f_z(-\partial L_z/\partial T)\rangle/[\chi_\perp(5.5/a)^2]^2}\right\}\right]}{2\langle \tfrac{1}{4}U_\alpha[\partial(\sigma v)/\partial T] + f_z(-\partial L_z/\partial T)\rangle} , \tag{1}$$

where

(σv) = fusion reactivity

U_α = 3.52 MeV

H = heating (positive) and atomic physics cooling (negative) terms

$n\chi_\perp = \kappa_\perp$

$\langle X\rangle$ brackets = $J_0(5.5r/a)$ − weighted volume average of X

$L \equiv f_z n^2 L_z(T)$ = impurity radiation cooling rate, with $f_z = n_z/n_i$ and L_z denoting the radiation emissivity function.

Note that a similar analysis assuming a uniform temperature collapse across the radius instead of a collapse that progressed inward from the outer regions would correspond to using $\mu = 2.4$, which would have to be represented by replacing 5.5 with 2.4 in expression (1).

A similar analysis of the coupled energy and particle balance equations with respect to instabilities in the radial temperature and density profiles led to a more involved expression for the maximum density for stability against radiative-driven instabilities:

$$n_{rc} \leq f^{-1}\frac{\{\hat{\chi}_\perp(5.5/a)^2\langle g\rangle + 2y[f_z\langle gL_z\rangle - \langle \tfrac{1}{4}U_\alpha g(\sigma v)\rangle]\}}{2\langle\{\tfrac{1}{4}U_\alpha[\partial(\sigma v)/\partial T] + f_z(-\partial L_z/\partial T)\}g^2\rangle} \times\left(1 \pm \sqrt{1 + \frac{4(\langle -\partial\hat{H}/\partial T\rangle - y\langle\partial\hat{H}/\partial n\rangle)\langle[\tfrac{1}{4}U_\alpha(\partial(\sigma v)/\partial T) + f_z(-\partial L_z/\partial T)]g^2\rangle}{\{\hat{\chi}_\perp(5.5/a)^2\langle g\rangle + 2y[f_z\langle gL_z\rangle - \langle \tfrac{1}{4}U_\alpha g(\sigma v)\rangle]\}^2}}\right) , \tag{2}$$

where

$n(r) = n_0 g(r)$

$f = n_0/n_{av}$ = peak-to-average value of the equilibrium density profile

y = effect of coupled density instabilities on the limiting density at which the equilibrium radial temperature profile is stable against radial collapse (given in Ref. 11).

The limiting density for thermal collapse predicted by these expressions increases with radial heat conductivity and decreases with impurity concentration when $\partial L_z/\partial T < 0$. Equation (2) correctly predicted a radial collapse of the temperature distribution in two DIII-D discharges,[13] which ended in disruption, but has not been broadly tested against experiment. It should be noted that a zero last closed flux surface (LCFS) boundary condition was assumed for the temperature perturbation and that taking into account temperature boundary condition perturbations[7] could modify the results of Eqs. (1) and (2).

As will be discussed subsequently, thermal collapse leading to disruption frequently follows some other thermal instability phenomenon such as MARFE formation,

detachment, or excessive cooling due to the accumulation of impurities, in which the term $\partial(H - L_z)/\partial T$ driving or stabilizing the radiative collapse in Eqs. (1) and (2) has a large value in a small spatial region (e.g., the edge) of the plasma. The $\tilde{T}(r) \sim J_0(5.5r/a)$ weighting of the spatial integrals denoted in Eqs. (1) and (2) by $\langle X \rangle$ attempt to take this into account.

Testing of radiative collapse threshold density predictions against experiment has been limited, and further work is needed in this area.

A linear stability analysis of the type leading to Eqs. (1) and (2) can only hope to predict the onset of the thermal collapse, of course; the nonlinear evolution must be investigated numerically.[14,15]

II.C. Mechanism for Coupling to Disruption

The scenarios postulated for the temperature profile collapse and current profile contraction due to thermal instabilities to cause a disruption involve triggering the $m/n = 2/1$ MHD mode by moving the steep part of the current profile into the region of the $q = 2$ surface. Kleva and Drake[16] have presented results supporting such a scenario. They included an impurity radiation model in a three-dimensional (3-D) MHD code and investigated the evolution of the temperature and current profiles. As the radiation increased, the calculated edge temperature dropped, and the calculated current profile contracted, forcing the edge current inward to produce a pronounced skin current. As the current profile further contracted, this skin current became larger and moved up the current gradient, successively destabilizing modes that were rational at progressively decreasing values of q (e.g., 2/1, 3/2, 4/3...). Ultimately, the skin current reached the top of the current profile, causing the minimum value of q to drop below 1 off-axis, destabilizing a $q = 1$ kink mode. This resulted in a bubble of cold plasma being injected into the central plasma by the $q = 1$ kink mode, producing a profile that was unstable to a broad spectrum of modes, which progressively reduced the magnetic shear between the $q = 2$ surface and the center. The $q = 2$ mode then grew across the center, broadening the current profile and ejecting hot plasma to the wall.

II.D. Radiating Mantle

Injection of low-to-intermediate-Z impurities, which would radiate copiously at the electron temperatures typically found in the edge plasma, has been demonstrated to result in up to ~90% of the power input to the plasma being radiated to the surrounding chamber walls.[17,18] While this result has obvious implications for reducing heat loads on limiters or divertor targets in future reactors,[17] and has been adopted as part of the power exhaust solution in ITER after extensive numerical simulation,[19–23] there are also obvious implications for the possibility of radiative collapse of the temperature profile leading to disruption. A few radiative collapse stability analyses have been performed,[10,12,24] but the stability of an impurity-seeded radiating mantle against radiative collapse is clearly an area needing further investigation.

II.E. Radiative-Accumulative Instabilities

Experiments related to the radiating mantle in the Axially Symmetric Divertor Experiment (ASDEX)-Upgrade[25–27] and the Tokamak Experiment for Technology Oriented Research[28,29] (TEXTOR) found critical parameters for the onset of central accumulation of intermediate-to-high-Z impurities. An injected power threshold was found in H-mode discharges in ASDEX-Upgrade, and a density limit was found in ohmic discharges in TEXTOR. Neon injection was also found to lead to central accumulation in neutral beam–heated discharges in TEXTOR.

Tokar et al.[30,31] offered an explanation for these observations by noting that the high-Z impurities were collisional and the temperature dependence of the Pfirsch-Schlüter (P-S) impurity flux could lead to an instability that caused the influx of impurities. A decrease in the temperature would produce an increase in the inward P-S impurity flux, causing an increase in the central impurity density and radiative power, resulting in a further decrease in the temperature, flattening the temperature profile or causing it to become hollow. Representing the radial impurity flux by a diffusive-pinch expression with the pinch proportional to the main ion density and temperature gradients, these authors performed a linear stability analysis of the radial temperature and impurity continuity equations to determine a threshold central plasma density above which the instability would be predicted to set in:

$$n^0_{thresh}(0) = \frac{8D_\perp \kappa_\perp T(0)}{r^2_{\max} D^{PS}_{neo} Z n_z L_z} \quad , \tag{3}$$

where

$$r_{\max} = \left(\frac{96 T D^2_\perp}{D^{PS}_{neo} Z n_z L_z} + \frac{1}{a^2} \right)^{-1/2} \quad ,$$

and they applied this expression to predict the onset of central impurity accumulation in TEXTOR ohmic discharges. For a given temperature profile, the expression (3) can be rewritten as a minimum central heating threshold condition below which accumulation sets in for an ohmic discharge:

$$\frac{8\kappa_\perp T(0)}{a^2} < \frac{r^2_{\max} D^{PS}_{neo}}{a^2 D_\perp} n n_z L_z \quad . \tag{4}$$

II.F. Current-Thermal Instabilities

As mentioned, Furth et al.[2] first studied the instability of the radial temperature profile caused by a temperature profile dependence of the inductive current profile in ohmic-heated plasmas. They found that the growth rate of the instability was the inverse plasma skin time and that the instability could be suppressed by fixing the total plasma current (i.e., the total heating rate). Putvinskii[32] extended this analysis to include the fusion alpha-particle heating and found that at fixed loop voltage the current-thermal instability was present over a wide range of conditions but again that at fixed current this current-thermal instability was suppressed. Kolesnichenko et al.[33] extended this work to consider noninductive currents and found current-thermal instabilities with growth rates that were the inverse of the plasma skin time.

Anderson et al.[34] further extended this line of investigation to consider currents driven by lower hybrid waves and neutral beams together with bootstrap currents. Using particle and energy balance equations and a current evolution equation, and taking the energy and particle confinement independent of temperature, they found that with lower hybrid current drive and using the International Thermonuclear Experimental Reactor (ITER) 89-P confinement scaling law, the current-thermal instabilities would be present. However, Engelmann[35] subsequently noted that had the required presence of plasma equilibrium control on the confinement timescale been taken into account, the current-thermal instability would be suppressed.

In summary, it seems that current-thermal instabilities are not likely to be a problem in auxiliary-heated tokamaks and can in any case be suppressed by controlling the total current.

III. MARFEs

III.A. Early Observations

The formation of regions of poloidally localized but toroidally symmetric, cool, dense plasma near limiters or divertor plates was initially observed in the early 1980s by Baker et al. in the Doublet III tokamak[36] (DIII) and subsequently by Alladio et al. in the Frascati Torus[37] (FT), by Niedermeyer et al. in ASDEX,[38] and by Kaye et al. in the Poloidal Divertor Experiment[39] (PDX). The dense plasma region formed when a threshold plasma density somewhat lower than the disruption density limit was exceeded. This threshold density was associated with the density that caused the temperature at the edge to decrease to the ionization energy of the recycling neutrals, making this mechanism the dominant heat transfer mechanism and resulting in a decrease in the heat flux through the edge with temperature $dQ/dT < 0$, which was argued to cause the scrape-off layer (SOL) to become unstable.[36] The high-density region appeared to be stable once formed, but if the plasma density was further increased, it expanded until the heat lost by the ionization of recycling neutrals exceeded the heat flow from the main plasma, at which point the plasma disrupted. This explanation in terms of recycling neutrals was elaborated theoretically by Tokar[40,41] and Nedospasov and Tokar.[42]

A similar edge plasma phenomenon was found by Lipschultz et al. in Alcator C (Ref. 43). However, it was found that the observed radiation of 20 to 30% of the input power could not be accounted for by plasma recycling at the limiter, but rather it was attributed to low-Z impurity radiation. The formation of these relatively small, poloidally localized, but toroidally symmetric, dense radiating bands was identified as manifestations of a thermal instability in the parallel energy balance, with impurity radiation being the major energy loss mechanism. A linear perturbation analysis led to the condition $dL_z/dT < -5\kappa_\parallel|\nabla T|/n_e n_z L_{T\parallel}$ for the onset of the cooling instability, with L_z being the impurity radiation cooling rate for carbon shown in Fig. 1 and $L_{T\parallel}$ being the parallel temperature gradient scale length. The name "multifaceted asymmetric radiation from the edge," or MARFE, was given to the cool, dense region. Subsequently, MARFEs were found in other tokamaks.[45–48]

Following the identification of the MARFE as an impurity radiative instability[43] (at least in some experiments), Stringer[49] and Neuhauser et al.[50] performed linear stability analyses of the one-dimensional (1-D) density, momentum, and energy balance equations along the field lines in the plasma edge, with a radiation loss term and a perpendicular heat conduction term, and derived an instability criterion

$$\kappa_\parallel k_\parallel^2 + \kappa_\perp/\Delta^2 + f_z n^2[(dL_z/dT) - (L_z/T)] < 0 \ , \quad (5)$$

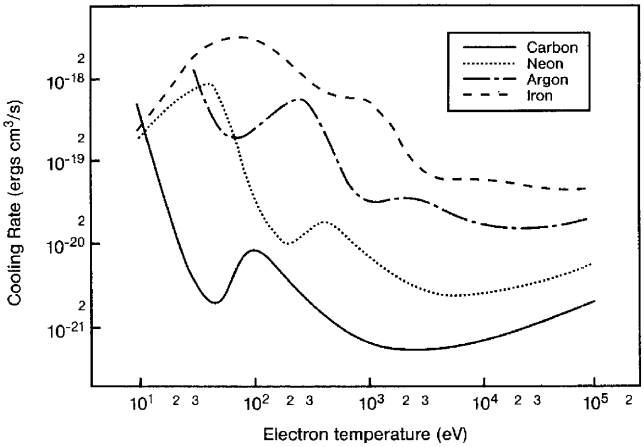

Fig. 1. Coronal equilibrium radiation emissivity function (calculated from ADPAC data[44]). Reprinted from Wiley-VCH with permission of Wiley-VCH.

where

$f_z = n_z/n_e$

$k_\parallel = (m/qR)$ for a temperature perturbation $\cos(m\theta)$

Δ = radial half-width of the perturbed edge layer.

Neuhauser et al.[50] also performed numerical studies that provided insight into the effect of the poloidal dependence of radial heat and particle fluxes into the plasma edge on the poloidal location of the MARFE.

III.B. Radiative Condensation Instability

Drake[51] was the first to suggest that MARFE formation was a radiative condensation process with an astrophysical precedent,[52,53] in which the temperature perturbation was coupled to a flow perturbation that in turn was coupled to a density perturbation. A local increase in plasma density increases the radiation rate, which reduces the local temperature, which requires the density to flow along field lines to further increase the density in the cool region ("condense") in order to maintain constant pressure along the closed field lines. He found that the edge plasma is unstable to thermal condensation when the radiation rate exceeds a critical value

$$L = n_z n L_z > 0.75 L_c \ , \tag{6}$$

where

$$L_c = (T_0/2T_L)H \ ,$$

where

H = heating rate in the central plasma

T_0 = plasma centerline temperature

T_L = temperature parameter associated with his radiation model, which assumes a constant radiation rate L_0 when the edge temperature is below T_L and zero radiation above T_L.

This model also predicts that L_c is the threshold radiation rate above which the radial temperature profile undergoes radiative collapse, so that the formation of a MARFE would be predicted to occur at a somewhat lower density than the radiative collapse leading to a disruption would occur, as is observed experimentally. The above relations can be rearranged to obtain a density limit for MARFE onset

$$n_{\mathrm{MARFE}} = [(\tfrac{3}{8})(T_0/T_L)(H/f_z)]^{1/2} \ . \tag{7}$$

Drake[51] further argued that when the density exceeded this value, the stabilizing effect of parallel heat conduction would inhibit the formation of a MARFE if

$$(\kappa_\parallel/n_{edge} q^2 R^2) > 0.48(T_0/T_L)^2/\tau_h \ , \tag{8}$$

where τ_h is the central heating time. It should be noted that expressions like Eq. (8), which contain a nonzero $k_\parallel \sim 1/qR$ term that essentially balances the parallel conductive heating of the perturbed parallel temperature distribution against radiation and other losses, are conditions for the stability of the perturbed MARFE distribution once it is formed, not stability conditions against the onset of MARFE formation, which proceeds from the unperturbed $k_\parallel = 0$ condition. This distinction notwithstanding, Eq. (8) was successfully applied to interpret the q-dependence of MARFE onset found in a couple of DIII-D shots,[54] a result probably owing more to the implicit q-dependence of the poloidal connection length for radiative cooling in the experiment than to the arguments leading to Eq. (8).

Drake's model was subsequently refined. Choudhury and Kaw[55] showed that taking into account the steep density variation in the edge increased the density limit of Eq. (7) and decreased the growth rate, while including ionization of neutrals in the radiation term stabilized the instability for large values of the radiation model parameter T_L and destabilized it for small values of T_L. Deshpande[56] demonstrated that Drake's results were recovered when a more realistic radiation model was used.

III.C. Threshold Conditions

The various conditions for MARFE onset outlined above constitute threshold conditions. There has been a considerable effort devoted to the further development of predictive models for the onset conditions of the MARFE instability. The general procedure has been to perform a linear analysis of a perturbation about a given equilibrium solution of the power and particle balance equations to obtain a dispersion relation for the growth rate of the perturbation and then to set the growth rate expression equal to zero to determine the threshold condition. Ross[57] has emphasized the necessity of using the equilibrium solution to incorporate a characterization of the equilibrium state into this type of stability analysis. This was not uniformly done in the earlier analyses.

It was apparent from the early work that both low-Z impurity radiation and atomic physics cooling due to recycling neutrals could be important in MARFE formation, to varying degrees depending on the experimental conditions. Most recent theoretical models include both, although represented in varying degrees of detail.

The theoretical explanation of MARFEs in terms primarily of recycling neutrals has been elaborated by Chen et al.,[58] Tokar et al.,[59,60] Tokar and Kelly,[61] Kelly and Tokar,[62] Samm et al.,[63] and others, who have developed a series of theoretical and computational models with an emphasis on elaborating the role in MARFE formation of ionization and charge exchange with recycling neutrals. The recent paper of Tokar and Kelly[61] is a good example of this line of development. These researchers developed a threshold condition for MARFE onset by performing a

linear perturbation analysis on the two-dimensional (2-D) (parallel and radial) particle and energy balance equations in the edge plasma, the neutral influx equation, and a wall recycling model. By approximating the radial ion and neutral flux gradients and integrating over the radial width of the edge region, they formally reduced the perturbed parallel heat flux equation to a 1-D Mathieu's equation, from the known form of the solution of which they were able to extract an expression for the growth rate of the perturbation, which was then set to zero to obtain a pair of transcendental equations:

$$n_{st} = n_* \sqrt{\frac{\dfrac{q_{core} L_T}{\kappa_\perp} - T_L}{3\tau T + E_i + Y E_{rad}}} \tag{9}$$

and

$$n_{cr} = n_* \sqrt{\frac{\xi_\Delta T_L}{E_*}} \ , \tag{10}$$

where

$n_* = [2\kappa_\perp \tau / D_\perp L_T \sigma_*]^{1/2}$

$\kappa_\perp \sim n^\varepsilon T^\varsigma, D_\perp \sim n^\eta T^\theta$ = plasma radial thermal conductivity and diffusivity, respectively

$\delta_T \equiv L_T$ = temperature gradient scale length

σ_* = characteristic cross section for attenuation of the recycling neutrals

$\tau = 2$

Y = effective impurity sputtering coefficient

q_{core} = heat flux from the plasma core into the edge

E_i = ionization energy of the recycling plasma neutrals

T = edge temperature

E_{rad} = radiation potential defined as the total energy radiated by an impurity particle during its time in the plasma

and $E_* = 3T_L(\xi_p - 1) + E_i \phi_i + Y E_{rad} \phi_{rad}$ is a complicated factor related to the recycling model, where

$$\phi_i = \xi_w \xi_p - \frac{d \ln E_i}{d \ln T} + \frac{d \ln E_i}{d \ln n} \ , \tag{11}$$

$$\phi_{rad} = \xi_p + \frac{d \ln \left(\dfrac{k_{ion}^{\mathrm{Li}}}{Y L_Z} \right)}{d \ln T} + \frac{\alpha}{\alpha + 1} \left[\frac{d \ln \left(\dfrac{k_{ion}^0}{V_0 \sqrt{k_{ion}^{\mathrm{Li}}}} \right)}{d \ln T} - \frac{1 - \theta_I + \eta_I}{2} \right] , \tag{12}$$

and

$$\xi_p = 1 - \frac{2 + \eta - \theta - \dfrac{d \ln \sigma_*}{d \ln T}}{2 - \xi_w} \ , \quad \xi_w = \frac{\gamma R_p + \mu}{\gamma + \mu} \ , \tag{13}$$

where

R_p = incident ion reflection coefficient

μ = desorption coefficient for neutrals trapped in the wall and diffusing back to the surface

k_{ion}^{Li} = rate coefficient for ionization into the Li-like state

k_{ion}^0 = rate coefficient for ionization of neutrals

V_0 = speed of the recycling neutrals

$\alpha = [n D_\perp / k_{ion}^{\mathrm{Li}}]^{1/2} (k_{ion}^0 / V_0)$

and

$$\xi_\Delta = 1 - \frac{\Delta_1^2}{\Delta_1 + \dfrac{2}{(1 + \varsigma - \varepsilon)} \dfrac{\tau \delta_{edge} L_T \kappa_\parallel}{q^2 R^2 \kappa_\perp}} \ , \tag{14}$$

where $\delta_{edge} = 1/n\sigma_*$ and $\Delta_1 = 2d\Delta/dr$, where Δ is the Shafranov shift at the boundary. The growth rate of the thermal instability perturbation is given by

$$\gamma \approx \frac{1}{5 n \delta_{edge}} \left[\frac{\Gamma_p E_*}{T} - \frac{\kappa_\perp}{\tau \delta_T} (1 + \varsigma - \varepsilon) \xi_\Delta \right] . \tag{15}$$

Equations (9) and (10) must be evaluated as a function of the edge n and T. The intersection of the curves $n_{cr}(n,T)$ and $n_{st}(n,T)$, if any, defines the threshold edge density n_{MARFE} and temperature T_{MARFE} at which the MARFE forms. Equations (9) and (10) have been evaluated for the conditions $q_{core} = 4$ W/cm^2, $\kappa_\perp = 2 \times 10^{20}$/s·m in TEXTOR, using recycling model parameters that have been developed and tested against TEXTOR results. The results with carbonized and boronized

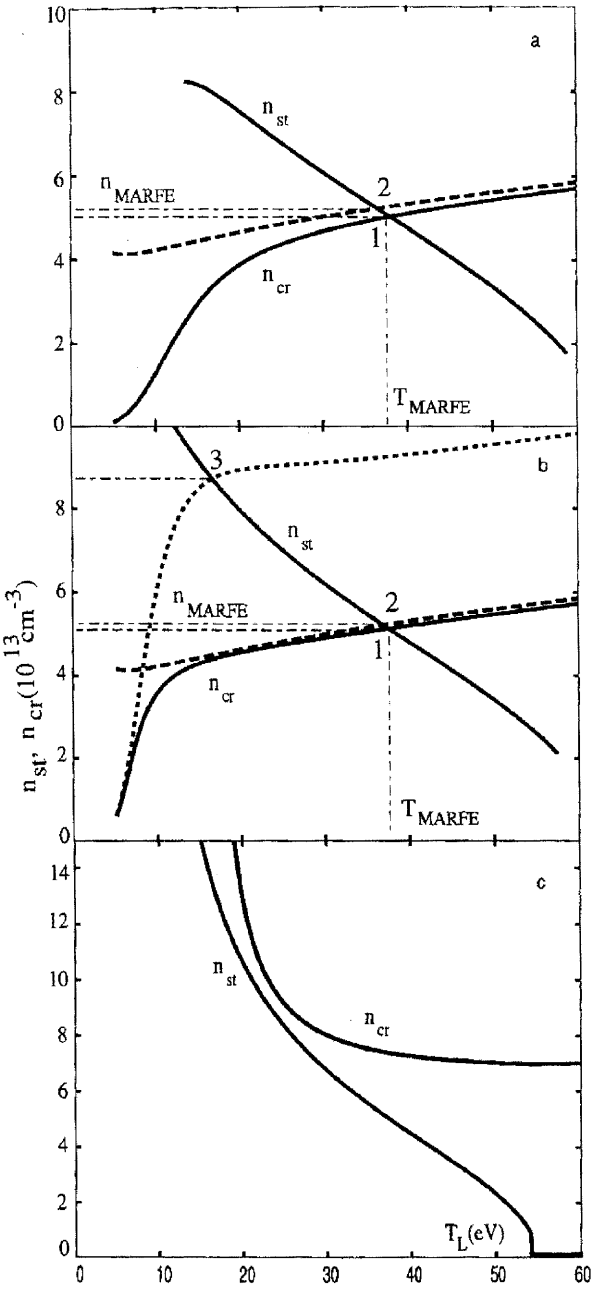

Fig. 2. Plot of Eqs. (9) and (10). Intersection points 1–3 identify edge plasma density and temperature at MARFE onset: (a) deuterium plasma in TEXTOR with carbonized wall, (b) deuterium plasma in TEXTOR with boronized wall, and (c) helium plasma in JET (Ref. 61). Reprinted from American Institute of Physics with permission of American Institute of Physics.

walls are shown in Figs. 2a and 2b, respectively. The solid curves, which include impurity and similar wall recycling neutral parameters for both cases, cross at point 1, defining the MARFE threshold density and temperature. The dashed curves, which only include recycling neutral effects (no impurity effects), cross at point 2. It is clear that the conditions for MARFE onset in this discharge are determined primarily by the recycling neutral-driven instability, which is represented by the recycling terms ϕ_i and ϕ_T in these calculations.

When the recycling coefficient was reduced to $R_p = 0.2$ to represent the more effective wall pumping of boronized walls, the recycling drive to the instability was significantly reduced, and the impurity drive became relatively more important. In this case, the dotted curve for n_{cr}, which crosses the n_{st} curve at point 3 in Fig. 2b, was obtained, indicating a much larger MARFE onset density with boronized walls, as found experimentally.[63]

These calculations clearly indicate that neutral recycling is the dominant cause of MARFEs in TEXTOR. Tokar,[40,41] Nedospasov and Tokar,[42] and Tokar et al.[59,60] had previously found a similar result for TEXTOR and other experiments. Chen et al.,[58] using Drake's model extended to include neutral recycling effects, also had previously found that neutral recycling effects were the dominant cause of MARFEs in model problem calculations with parameters similar to TEXTOR. Samm et al.[63] and Rapp et al.[64] came to a similar conclusion about the importance of neutral recycling for MARFE formation in TEXTOR. Figure 2c shows the evaluation of Eqs. (9) and (10) for a He plasma in JET ($q_{core} = 3.5$ W/cm^2, $\kappa_\perp = 1 \times 10^{20}$/s·m, $L_T = 3$ cm). There is no intersection of the two curves, indicating no MARFE formation, in general agreement with experiment for He plasmas in JET.

A different theoretical MARFE threshold condition was developed by Stacey,[65–67] who performed a linear stability analysis on the reduced 3-D $(r, \perp, \|)$ fluid energy, momentum, and particle balance equations in the plasma edge (radial convection, parallel currents and electric fields neglected, impurities entrained to move with plasma ions). The general time-dependent solutions of these equations were expanded about equilibrium solutions in the form $T'(r, l_\|, t) = T(r) + \delta T \exp(\omega t + i[k_\| l_\| + k_r r])$, where $k_\| = (m + nqB_\theta/B_\varphi)/qR$ represented perturbations periodic in poloidal and toroidal coordinates (m and n are the poloidal and toroidal mode numbers). Similar expansions were made for $v_\|$ and n. Linearizing the resulting equations and using the equilibrium form of the equations to incorporate the equilibrium solution into the stability analysis led to a dispersion relation for $\mathrm{Re}(\omega)$, the growth rate, which was used to determine the stability condition $\mathrm{Re}(\omega) < 0$:

$$n_z\left((\nu + K_1)\frac{L_z}{T} - \frac{\partial L_z}{\partial T}\right) - \frac{3}{2}\nu_s\left(\frac{T}{\nu_s}\frac{\partial \nu_s}{\partial T} + 1 - \nu\right) - \frac{E_{ion}}{T}\nu_{ion}\left(\frac{T_{ion}}{\nu_{ion}}\frac{\partial \nu_{ion}}{\partial T} + 1 - \nu\right) - 5T\frac{\partial \nu_n}{\partial T} \le (k_r^2 + L_T^{-1}(\nu L_T^{-1} - K_1 L_n^{-1}))\chi_\perp + (k_\|)^2\chi_\| \ , \quad (16)$$

where ν represents the temperature dependence of the radial thermal conductivity, $\chi_\perp \sim T^\nu$, and the condensation effect is represented by the term

$$K_1 = 1 - \left[\frac{4}{3}\tau_{ii} + \nu_s \left(\frac{1}{k_\parallel c_s} \right)^2 \right] T \frac{\partial \nu_n}{\partial T} \quad , \qquad (17)$$

where $\nu_n = \nu_{ion} - \nu_{rec}$ and $\nu_s = \nu_{cx} + \nu_{el}$.

Equation (16) with the equality is the threshold condition for MARFE onset, and with the inequality it is the condition for stability. The conductive terms $(k_r^2 + \nu L_T^{-2})\chi_\perp$ and $k_\parallel^2 \chi_\parallel$ on the right are always positive (the range $1.5 < \nu < 3.5$ is assumed[68]), hence stabilizing. This result of the stabilizing nature of heat conduction is generally consistent with the work of previous authors, e.g., Refs. 49, 50, 51, 55, 56, 69, 70, and 71.

Inclusion of rotation effects into the stability analysis[66] indicates that parallel rotation stabilizes parallel instabilities and thus would be expected to increase the MARFE density limit. This suggests a possible explanation of the observation of increased density limits in TEXTOR discharges operated in the alternative current mode, which drives parallel flows.[72]

The impurity radiation and atomic physics cooling terms on the left side of Eq. (16) can be positive or negative, depending on the edge temperature. If $dL_z/dT < 0$, then the impurity radiation term is positive, and even if $dL_z/dT > 0$ but small relative to L_z/T, the impurity radiation term could still be positive. If the impurity radiation term is positive and larger than the conductive heating term on the right, then the impurity radiation drive would be large enough to cause a MARFE to form. With reference to Fig. 1, a carbon impurity would be a strong radiation drive for $10 < T < 50$ eV and $100 < T < 1000$ eV but not such a strong drive for $T < 10$ eV or $50 < T < 100$ eV. If $\nu > 1 (\chi_\perp \sim T^\nu)$, then the atomic physics cooling terms in Eq. (16) are positive and could also be larger than the conductive heating term and cause a MARFE to form.

There are two important phenomena that are not included in the coronal equilibrium calculations on which Fig. 1 is based. First, in the presence of recycling neutrals, charge-exchange and recombination processes between partially stripped impurity ions and neutral hydrogen atoms greatly enhance the impurity radiation cooling rate for higher edge electron temperatures ($T > 10$ eV for carbon,

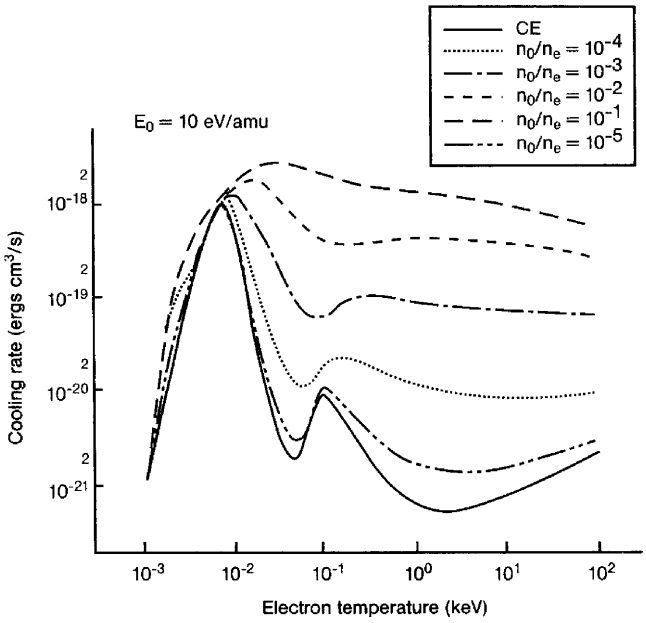

Fig. 3. Effect of charge exchange and recombination with neutral hydrogen atoms on the carbon radiation emissivity function.[73] Reprinted from Wiley-VCH with permission of Wiley-VCH.

as shown in Fig. 3). This effect strengthens the L_z/T part of the radiative drive term but weakens the negative dL_z/dT part; the overall effect is generally to strengthen the impurity radiative drive for the MARFE instability.

The second important effect that has not been taken into account in Fig. 1 is the effect of transport from nearby regions with different electron temperatures on the local impurity charge state distribution [the coronal equilibrium (CE) calculation neglects this transport as being slow compared with the ionization and recombination rates]. This is a complex matter, and preliminary investigations[74,75] indicate that treating the noncoronal effect is important but have found different results regarding whether the impurity drive is weakened or strengthened by doing so.

Equation (16) can be converted into a threshold edge density for MARFE onset of the mode with a given $k_\parallel$ by using $f_z = n_z/n$, $f_0 = n_0/n$, and $f_0^c = n_0^c/n$ (c refers to "cold" neutrals that have not previously collided in the edge plasma) to write

$$n_{\max}(k_\parallel) = [\chi_\perp \nu L_T^{-2} + \chi_\parallel k_\parallel^2 - K_1 \chi_\perp L_T^{-1} L_n^{-1}] \div \left[f_z \left\{ (\nu + K_1) \frac{L_z}{T} - \frac{\partial L_z}{\partial T} \right\} + \left[f_0 \frac{E_{ion}}{T} \langle \sigma v \rangle_{ion} \left(\nu - \frac{T}{\langle \sigma v \rangle_{ion}} \frac{\partial \langle \sigma v \rangle_{ion}}{\partial T} \right) \right.\right.$$
$$\left. + f_0^c \frac{3}{2} (\langle \sigma v \rangle_{cx} + \langle \sigma v \rangle_{el}) \left(\nu - 1 - T \frac{\partial (\langle \sigma v \rangle_{cx} + \langle \sigma v \rangle_{el})/\partial T}{(\langle \sigma v \rangle_{cx} + \langle \sigma v \rangle_{el})} \right) \right]$$
$$\left. + \frac{5T \partial (f_0 \langle \sigma v \rangle_{ion} - \langle \sigma v \rangle_{rec})}{\partial T} \right] . \qquad (18)$$

The first f_z term in the denominator represents the low-Z impurity drive for the MARFE instability, and the second, f_0 and f_0^c, terms represent the neutral atomic physics drive for the MARFE instability. Condensation (K_1) reduces the threshold density both by increasing the impurity instability drive and by reducing the heat conduction stabilization term.

The atomic physics terms on the left side clearly depend on the temperature dependence of the various cross sections ($\nu_x = n_0\langle\sigma_x v\rangle$); $\langle\sigma_{cx}v\rangle$ and $\langle\sigma_{el}v\rangle$ vary only by a factor of ~3 between $T = 1$ eV and $T = 100$ eV, so the $(T/\nu_s)(d\nu_s/dT)$ term is not important. On the other hand, $\langle\sigma_{ion}v\rangle$ and $\langle\sigma_{rec}v\rangle$ vary by six orders of magnitude between 1 and 10 eV, as shown in Fig. 4. The $-f_0 E_{ion}(d\langle\sigma v\rangle_{ion}/dT)$ term is large and negative over $1 < T < 10$ eV and thus increases the maximum edge density for MARFE onset (stabilizing), but the $5T(d(f_0\langle\sigma v\rangle_{ion} - \langle\sigma v\rangle_{rec})/dT)$ term is large and positive (destabilizing) over $1 < T < 10$ eV, suggesting the possibility of an ionization-recombination–driven MARFE, which has actually been observed, as will be discussed later. Both terms can be neglected for $T \gg 10$ eV. The $\langle\sigma v\rangle_{ion}(E_{ion}/T)\nu$ and $3/2(\langle\sigma v\rangle_{cx} + \langle\sigma v\rangle_{el})(\nu - 1)$ terms are neutral recycling MARFE instability drivers associated with the positive temperature dependence of $\chi_\perp \sim T^\nu, \nu > 0$.

Clearly, modes with larger $k_\parallel = (m + nqB_\theta/B_\phi)/qR$ have progressively larger threshold densities for instability onset, and $k_\parallel \approx 0$ modes have the lowest threshold density, because the parallel thermal diffusivity is large and the stabilizing term $k_\parallel^2\chi_\parallel$ appears in the numerator of Eq. (18). A conservative estimate for the threshold density for the onset of a MARFE instability is obtained by setting $k_\parallel = 0$ to eliminate the stabilizing conduction term but retaining the destabilizing condensation (K_1) term in Eq. (18) to obtain $n_{\text{MARFE}} = n_{\max}(k_\parallel = 0)$, which is given explicitly by

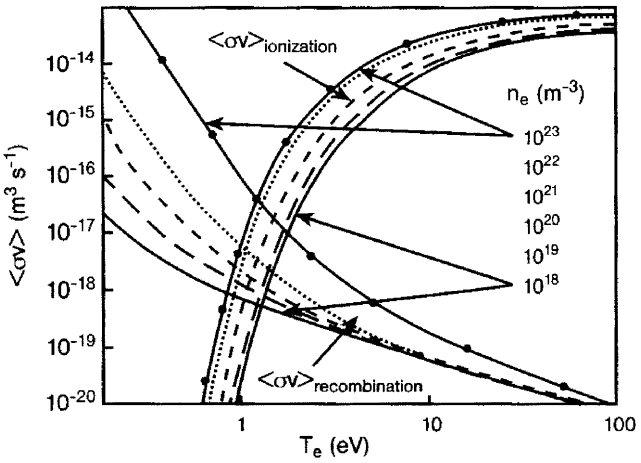

Fig. 4. Ionization and recombination $\langle\sigma v\rangle$ for hydrogen.[73] Reprinted from Wiley-VCH with permission of Wiley-VCH.

$$n_{\text{MARFE}}^2 = \frac{f_{cond}Q_\perp}{T}\left[\nu L_T^{-1} - K_1 L_n^{-1}\right] \div \left[f_z\left\{(\nu + K_1)\frac{L_z}{T} - \frac{\partial L_z}{\partial T}\right\} + f_0\frac{E_{ion}}{T}\langle\sigma v\rangle_{ion}\left(\nu - \frac{T}{\langle\sigma v\rangle_{ion}}\frac{\partial\langle\sigma v\rangle_{ion}}{\partial T}\right)\right.$$
$$+ f_0^c\frac{3}{2}(\langle\sigma v\rangle_{cx} + \langle\sigma v\rangle_{el})\left(v - 1 - T\frac{\partial(\langle\sigma v\rangle_{cx} + \langle\sigma v\rangle_{el})/\partial T}{\langle\sigma v\rangle_{cx} + \langle\sigma v\rangle_{el}}\right)$$
$$\left. + \frac{5T\partial(f_0\langle\sigma v\rangle_{ion} - \langle\sigma v\rangle_{rec})}{\partial T}\right], \tag{19}$$

where the conductive heat flux relation $f_{cond}Q_\perp = q_\perp = nT\chi_\perp L_T^{-1}$ has been used and f_{cond} is the conductive fraction of the total radial heat flux $Q_\perp$ across the plasma edge.

Based on Eq. (19), the threshold edge density for MARFE formation increases with the conductive heat flux across the edge (hence with the auxiliary heating power) and with the steepness of the temperature gradient ($L_T^{-1} = (-dT/dr)/T$) in the edge and decreases with the impurity and neutral concentrations. The decrease with neutral concentration is not only the explicit one shown in Eq. (19) but also the increase of $L_z(f_0, T)$ due to charge-exchange and recombination reactions involving the impurity ions and the recycling neutrals. The temperature dependence is more complex; there is an explicit $n_{\text{MARFE}}^2 \sim 1/T$ dependence, but there is also the temperature dependence of L_z shown in Fig. 1 and the temperature dependencies of the atomic physics $\langle\sigma_x v\rangle$.

Equation (19) was evaluated[76] for a series of TEXTOR-94 shots in a power scan sequence over which the measured edge densities at MARFE onset increased from 5.8×10^{18} to 9.4×10^{18}/m^3 and the measured edge temperatures increased from 28 to 35 eV with increasing auxiliary power. The carbon edge impurity concentrations varied from 1.2 to 1.6%, and the oxygen edge impurity concentration was estimated to be 0.13 times the carbon concentration. The neutral concentrations were calculated from experimentally determined recycling sources, and the attenuation into the edge plasma was calculated numerically; the edge neutral concentrations varied from 0.55 to 0.92%. The ratio [MARFE index (MI)] of the measured edge density at the time of MARFE formation to the MARFE

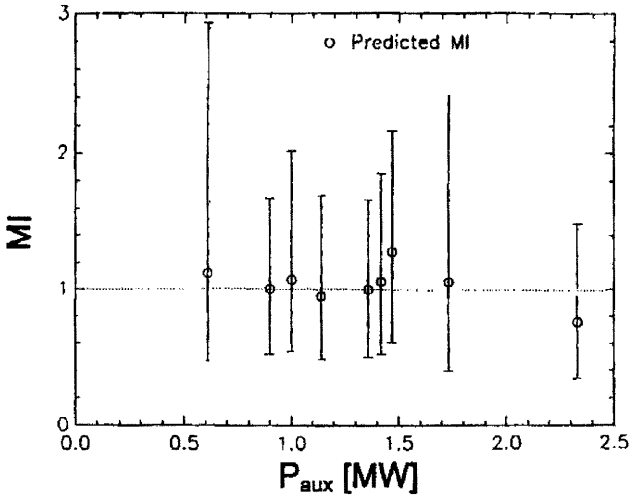

Fig. 5. MARFE index—ratio of measured edge electron density at MARFE onset to the predicted threshold edge density for MARFE onset from Eq. (19)—for a TEXTOR power scan.[76] Reprinted from American Institute of Physics with permission of American Institute of Physics.

threshold density n_{MARFE} predicted from Eq. (19) is shown in Fig. 5. The combined uncertainty in the prediction [due to uncertainty in measurements used to evaluate Eq. (19) and to the uncertainty in the measured edge density] is also shown. The impurity radiation drive (the f_z term) and the recycling neutral drive (the f_0 terms) were found to be of comparable importance in causing the MARFE formation in this series of TEXTOR experiments.

The MARFE threshold model of Eq. (19) has been extended to allow equilibrium solutions with poloidal asymmetry and rotation[77] and MARFE suppression by edge heating,[78] to confirm the impurity entrainment assumption,[79] and to incorporate the effects of heat convection.[80]

III.D. Detachment

In the process of studying MARFEs, a new poloidally symmetric edge radiation phenomenon, the detached plasma, was found by Allen et al.[81] and McCracken et al.[82] in DITE, Samm et al.[83] in TEXTOR, Strachan et al.[84] and Boody et al.[85] in the Tokamak Fusion Test Reactor (TFTR) and subsequently in other experiments. The detached plasma condition was characterized by a thin poloidally and toroidally uniform, highly radiating region at the plasma edge. All of the input power was radiated, the heat and plasma particle flow to the limiter vanished, and the plasma radius was less than the limiter radius.

In TEXTOR, when subjected to continuous fueling, the ohmic-heated and the high-Z_{eff} auxiliary-heated discharges tended to detach symmetrically when the radiated power reached 100% of the input power and then undergo a radiative collapse of the temperature profile and disrupt,[86] whereas the auxiliary-heated discharges and the low-Z_{eff} ohmic-heated discharges (with siliconized walls) tended to first form MARFEs (Refs. 87 and 88) and then undergo radiative collapse and disruption.

An interesting sequence was observed in TFTR, where a MARFE first formed in a poloidally symmetric edge plasma, cooling the plasma edge and causing the plasma radius to shrink and the plasma to pull away from the limiter, at which point the MARFE spread poloidally to become a thin cylindrical shell that was poloidally and toroidally symmetric.[89] The plasma edge temperature in the detached state was ~10 eV. With respect to the linear instability model, this sequence of events is consistent with the MARFE threshold density of Eq. (19) initially being exceeded and then the plasma edge cooling down sufficiently quickly once the MARFE started to form that the MARFE density limit ($n^2_{\mathrm{MARFE}} \sim 1/T$) increased above the actual edge density before the MARFE could fully develop, at which point the MARFE instead evolved into a poloidally symmetric detached plasma.[65] This observation is also consistent with the results of Kaw et al.,[90] who solved a 2-D nonlinear heat conduction problem where perpendicular and parallel heat conduction into an initially poloidally asymmetric radiating (MARFE) region balanced the radiation from this region and the heat flux to the limiter. They found that the asymmetric highly radiating region evolved into a poloidally symmetric band and the heat flux to the limiter diminished; i.e. the plasma approached detachment.

Tokar[91] modified Drake's radiative condensation model[51] to include a temperature gradient boundary condition at the LCFS determined from the competition between parallel and perpendicular heat flows in the SOL, instead of a fixed temperature (usually $T = 0$) boundary condition. He then performed a linearized perturbation analysis to determine the growth rate of the thermal instability, which was set equal to zero to determine the threshold density for detachment:

$$n_{det} = f_{cond} Q_\perp / [k_\perp T_L f_z L_0 (1 + \{1 - L_T^2/\delta_0^2\}^{1/2})]^{1/2} \quad , \tag{20}$$

where $\delta_0 = \kappa_\perp T_L / f_{cond} Q_\perp$; T_L is a temperature parameter associated with the radiation model, which assumes a constant radiation rate L_0 when the edge temperature is below T_L and zero radiation above T_L. This critical density for the onset of plasma detachment has a parameter dependence similar to that of the MARFE threshold density of Eq. (19); n_{det} increases with conductive heat flux from the core into the edge and with the temperature gradient L_T in the edge, decreases with the impurity radiation strength $f_z L_0$, and has an explicit $n_{det} \sim 1/T^{1/2}$ dependence.

One might expect that neutral recycling and volumetric recombination, which were not included in the analysis leading to Eq. (20), play an important role in the detachment process. The effects of neutral recycling could be approximately included in Eq. (20) by adding to the impurity radiation strength $f_z L_0$ a neutral cooling term of the form $f_0 L_{neut}$ [e.g., as in the denominator of Eq. (19)].

III.E. Diverted Plasmas

In the interplay of MARFEs, detachment and thermal collapse leading to disruption are different in diverted plasmas than previously discussed for limited plasmas. The typical sequence of events that is observed when the density is increased by continuous gas fueling in a diverted, H-mode plasma has been well documented for DIII-D (Refs. 92 through 95):

Event 1: The plasma partially detaches (complete detachment near the separatrix strike point on the divertor target and significantly reduced power and particle fluxes to the remainder of the divertor target), and a dense, radiating region forms just in front of the target.

Event 2: With continued fueling the density in front of the divertor target is suddenly reduced, and a dense, cool radiating region (a "divertor MARFE") is formed upstream in the vicinity of the *X*-point but outside the separatrix, or LCFS, on open field lines.

Event 3: With continued fueling the divertor MARFE gradually moves inward across the separatrix to form a MARFE on closed field lines in the vicinity of the *X*-point (an "*X*-point MARFE"), and immediately thereafter event 4 occurs.

Event 4: The plasma makes a back transition from H-mode to L-mode confinement.

A similar sequence of events has been documented for ASDEX-U (Ref. 96), JET (Ref. 97), JT60-U (Ref. 98), Alcator C-Mod (Ref. 99), and other diverted tokamaks, as surveyed by Matthews.[100] Thus, the eventual outcome of detachment and MARFE formation in a diverted plasma is a stable plasma with L-mode confinement, although continued gas fueling would lead eventually to a thermal collapse and disruption.

It is generally possible to arrest the above sequence of events at any stage prior to *X*-point MARFE formation by some combination of termination of gas fueling, pumping, etc., to achieve stable operation of a detached plasma. Stable operation of detached divertor plasmas with confinement and other properties comparable to or better than attached plasmas has been accomplished in ASDEX-U (Ref. 101), Alcator C-Mod (Ref. 102), DIII-D (Ref. 103), and other tokamaks. Two-dimensional edge fluid codes have been successful in reproducing many observed features of detached plasmas in DIII-D (Ref. 104), ASDEX-U (Refs. 105 and 106), JET (Ref. 107), JT60-U (Refs. 108 and 109), Alcator C-Mod (Ref. 110), and other diverted tokamaks, as surveyed by Loarte.[111] The necessity for volumetric recombination near the target plate to explain detachment in a JET diverted plasma was first predicted by Borrass et al.[112] and then measured by McCracken et al.[113]

The conditions for the *X*-point MARFE formation inside the separatrix appear to be well described by the thermal instability model leading to Eq. (19) described above, when account was taken of the long path length in the vicinity of the *X*-point of field lines just inside the separatrix when performing a flux-surface average of the neutral density. Stacey and Petrie[13] and Stacey et al.[114–116] evaluated Eq. (19) using measured plasma edge parameters and edge impurity concentrations and neutral concentrations calculated with a 2-D neutral recycling model for those conditions, for a number of times during several "density limit" discharges with continuous gas fueling in DIII-D. They found that the time at which the increasing value of the measured edge density became as large as the calculated MARFE threshold density n_{MARFE} was very close to the time t_{MARFE} at which the *X*-point MARFE formation was observed experimentally, as shown in Table I. Similar discharges in which MARFEs were neither observed nor predicted are indicated by "none." (The divertor MARFE onset shown in Table I will be discussed later.)

It is noted that the MARFE onset prediction of Eq. (19) has no explicit q_{95}-dependence. Yet, it is clear from Table I that the line average density at which a MARFE occurred, normalized to the Greenwald density $n_{GW} = \mathrm{I}/\pi a^2$, depended inversely on q_{95} and that Eq. (19) predicted this dependence. The likely explanation is that some of the measured edge parameters that were used to evaluate Eq. (19) depend on the parallel path length of the SOL and divertor channel along the field lines and this path length can be characterized by $L_\parallel \sim q_{95}$; e.g., the longer $L_\parallel$ the more radiative and recycling neutral cooling and the lower the edge temperature, other things being the same.

III.F. Role of Parallel Heat Conduction

While there is general agreement that perpendicular (radial) heat conduction is important in the determination of the MARFE threshold condition, the role of parallel conduction is more ambiguous. The early work, e.g., Refs. 49, 50, 51, and 70 emphasized the $k_\parallel^2 \chi_\parallel$ term because of the large value of $\chi_\parallel$ but also retained the $L_T^{-2} \chi_\perp$ term in defining MARFE onset conditions. However, the parallel heat conduction does not come into play in a poloidally uniform ($dT/dl_\parallel = 0$) plasma edge prior to initiation of MARFE formation.

The threshold density estimate of Eq. (19) should be conservative (low) because the stabilizing effect of the parallel heat conduction has been suppressed, but the destabilizing effects of condensation (the K_1 terms) have been retained. (Had the stability analysis been performed

TABLE I

MARFE Onset Prediction for Gas-Fueled DIII-D Shots

Shot Number	P_{NB} (MW)	q_{95}	n/n_{GW} at t_{MARFE}	MARFE t^{exp}_{MARFE} (s)	MARFE t^{calc}_{MARFE} (s)	Divertor MARFE $t^{exp}_{DIVMARFE}$ (s)	Divertor MARFE t at $\omega_{div} > 0$ (s)
92980	9.5	6.0	0.73	3.53	3.5 to 3.6		
92976	5.0	6.0	0.67	3.05 to 3.10	3.0 to 3.2	2.70 to 2.90	2.70 to 2.75
92983	2.5	6.0	0.58	2.90 to 3.00	2.6 to 2.8		
92972	5.0	3.0	0.95	3.05 to 3.15	3.0 to 3.2		
97979	6.5	3.8	0.81	None	None		
100308	4.5	3.1	0.96	None	None		
98893	2.0	3.5	1.40	None	None		
101560	4.6	4.2	0.79	4.80 to 4.90	4.8 to 4.9	4.65 to 4.80	4.50 to 4.80
101565	4.7	4.0	0.80	4.80 to 4.90	4.8	4.60 to 4.85	4.60 to 4.80
101626	3.4	4.2	0.81	None	None	None	None
101627	4.8	4.2	0.75	None	None	None	None
102447	4.5	4.0	0.79	4.90 to 4.98	4.8 to 4.9	4.70 to 4.90	4.80 to 4.90
102858	4.5	4.3	0.77	3.90 to 4.53	4.2 to 4.4	4.10	4.00 to 4.20
102859	4.7	4.1	0.74	4.10 to 4.25	4.0 to 4.2	4.10 to 4.30	4.0
102461	2.5	2.9	0.95	None	None		
102456	2.5	3.9	0.79	3.30 to 3.33	3.30 to 3.33		

*References 13, 114, 115, and 116. $R = 1.70$ to 1.76 m, $a = 0.6$ m, and $\kappa = 1.70$ to 1.75.

with $k_\parallel = 0$ from the outset, both the parallel conduction and the condensation effect would be absent.) This procedure of estimating the threshold edge density from $n_{MARFE} = n_{max}(k_\parallel = 0)$ is supported by the results of multimode (n, m) dynamic simulations of JET (Ref. 117), which found that the MARFE formation was initiated by the $(m = 0, n = 0, k_\parallel = 0)$ mode first going unstable to produce uniform edge cooling. This unstable mode then triggered other $k_\parallel \approx 0$ modes, which in turn triggered $k_\parallel \neq 0$ modes that evolved into a stable MARFE. Sensitivity studies revealed that the calculated MARFE onset condition and growth rate were more or less independent of which (m, n) modes were included in the calculation, provided only that the $(m = 0, n = 0, k_\parallel = 0)$ mode was included. Based on the above analytical results and this numerical result, the choice of a MARFE threshold condition $n_{MARFE} = n_{max}(k_\parallel = 0)$ that does not depend on parallel heat conduction seems justified for a poloidally symmetric plasma model. The analysis of Ref. 117 was based on a coupled set of energy and particle balance equations and the ideal MHD equations, of which the latter are questionable in the plasma edge, but the results indicated little coupling between distinct sets of thermal modes and MHD modes, so the thermal mode results discussed above were apparently not affected by the ideal MHD treatment.

As contrasted to the analysis leading to Eq. (19) used above, which was based on an effective cylindrical model of the plasma inside the separatrix, Igitkhanov and Mikhailov[118] undertook an analysis of MARFEs on closed field lines in a configuration with an x-point, taking into account flux expansion near the x-point. They used a "ballooning" perturbation with long parallel and short perpendicular wavelengths to represent the MARFE and concluded that parallel (as well as perpendicular) heat conduction is important because of geometry effects.

Tokar[119] showed that the critical radiation loss and plasma density for MARFE onset increased with increasing parallel heat conductivity, but in the limit of very high $\kappa_\parallel$, the threshold is independent of $\kappa_\parallel$ and depends only on $\kappa_\perp$.

III.G. Ionization-Recombination Instability

An ionization-recombination instability has been suggested as the thermal instability mechanism for the formation of MARFEs in situations in which the temperature just inside the LCFS is extremely low. This phenomenon arises from the very strong temperature dependence of the ionization (positive) and recombination (negative) rate coefficients at temperatures around 1 eV, which is shown in Fig. 4. The instability might be initiated by a negative temperature perturbation at the low-temperature end of the ionization region, which would reduce the ionization rate and increase the volumetric recombination rate, resulting in a negative perturbation in the plasma density and a positive perturbation in the neutral density. The original negative temperature perturbation and the secondary negative density perturbation would require a plasma influx to maintain parallel pressure balance along the field lines, which would increase the local plasma density after a short delay $\tau_\parallel^n$.

The original negative temperature perturbation would also cause a conductive heat influx, which would increase the temperature at a time $\tau_{\|}^{T}$ later. The stability/instability would depend on the competition between the stabilizing heat conduction effects and the destabilizing ionization-recombination effects, as indicated in the threshold condition of Eq. (19).

Morozov and Herrera[120] first suggested the possibility of an ionization-recombination instability. MARFEs were subsequently found in ALCATOR C-Mod by Lipschultz et al.[121] and by Samm et al.[63] and Sergienko et al.[122] in TEXTOR under conditions ($T < 1$ eV) at which low-Z impurity radiation would be ineffective but the ionization-recombination instability would be expected to be important. There was experimental evidence of strong recombination in the MARFE region. A theoretical treatment of this phenomenon was elaborated by Tokar et al.[59] and by Krasheninnikov et al.[123] and Simakov and Krasheninnikov.[124] The latter authors[124] found that volumetric recombination increases the ionization-recombination instability at temperatures near 1 eV but did not take into account the stabilizing effect of three-body recombination, while the former authors[59] explained the stability of MARFEs in the 1-eV range by the reduced rate of increase in neutral penetration depth with temperature for T below the ionization potential.

III.H. Poloidal Location

The MARFE location in limited discharges has been generally on the inboard, high-field side of the tokamak.[48] On ASDEX, FT, and DIII, the MARFE was centered on the inboard midplane ($\theta = 180$ deg), but in Alcator-C, JET, and TFTR with the $\mathbf{B}x\nabla B$ direction up, the MARFE was centered in the upper inboard quadrant at ~235 deg (measured clockwise relative to the outboard midplane). In JET and TFTR, the MARFE first appeared in the lower inboard quadrant at ~125 deg, then with increasing density moved upward to a symmetric location ($\theta = 235$ deg) above the midplane; the symmetry of the process could be reversed by reversing the magnetic field direction.

In diverted tokamak plasmas,[48,125,126] the MARFE usually formed first in the x-point region. If the grad-B drift direction was toward the x-point, the stable MARFE remained at the x-point. If the grad-B drift direction was away from the x-point, the MARFE moved around the high-field (inboard) side to the midpoint of the opposite quadrant; e.g., in a lower-single-null (LSN) divertor with the x-point at the bottom and the grad-B drift up, the MARFE formed at the bottom and moved up the inboard side above the midplane to $\theta = \sim 235$ deg.

There are several theoretical factors that should affect the location of the MARFE. It is generally thought that propensity for MARFE formation on the high-field inboard side was due to a higher heat flux going to the outboard than to the inboard side. This would result in a lower value of the threshold density for MARFE formation given by Eq. (19) on the inboard, high-field side. Neuhauser et al.[50] and Singh et al.[127] have also demonstrated by numerical calculations that MARFEs have a propensity to form in regions of low perpendicular conductive heat flux. Equation (19) also indicates that MARFEs would have a propensity to form in regions of high neutral concentrations, i.e., near a limiter or the x-point where recycling neutrals would tend to enter the plasma edge. Chankin[128] showed that the poloidal $E \times B$ drift, with $E_r < 0$, creates poloidal rotation that displaces the MARFE in the grad-B drift direction. The outboard bias of the radial conductive heat flux and the $E \times B$ drift effects account qualitatively for the observed locations in limited plasmas, and these two factors plus the high neutral recycling in the x-point region account qualitatively for the observed locations in diverted plasmas.[129]

Tokar et al.[59] showed that in the case of small $\kappa_{\|}$, the MARFE instability develops first on the high-field side of limited discharges where the separation between magnetic surfaces is largest because of the Shafranov shift. Such effects of the magnetic geometry are not taken into account in Eqs. (16) through (19).

III.I. Evolution

Several researchers have studied the evolution of the MARFE from a poloidally uniform edge to a poloidally asymmetric but toroidally uniform cool, high-density band. DePloey et al.[117,130] expanded solutions of the perturbed particle, momentum, and energy balance equations in toroidal eigenfunctions

$$T'(r,\theta,l_{\|},t) = T(r) + \sum_{m,n} \delta T_{nm}(r,t)\exp(i[m\theta + k_{\|}l_{\|}]) \ ,$$

where $k_{\|} = (m + nqB_{\theta}/B_{\varphi})/qR$, used similar expansions for the perturbed density and parallel velocity, integrated over the flux surface with similar harmonic weighting functions, and made use of the orthogonality relations to develop coupled equations for the $\delta T_{nm}(r,t)$, $\delta n_{nm}(r,t)$, and $\delta v_{nm}(r,t)$, which were then solved numerically. They found for a JET calculation that the MARFE was initiated by a uniform edge cooling mode ($k_{\|} = n = m = 0$) first going unstable. This mode first coupled to other approximately uniform ($k_{\|} \approx 0$, $n \neq 0$, $m \neq 0$) modes, and then to nonuniform ($k_{\|} \neq 0$, $n \neq 0$, $m \neq 0$) modes, primarily ($n = 0$, $m = \pm 1$).

Other researchers have simulated the evolution of MARFEs with 2-D plasma fluid edge codes. Kastelewicz et al.[131] found that a steady-state MARFE in ASDEX-U is sustained in a dynamic way by a complex 2-D pattern of parallel and radial particle, momentum, and energy fluxes. Zagorski et al.[132] demonstrated that MARFEs could be triggered in TEXTOR-94 by localized neutral recycling when the LCFS was sufficiently close to the

bumper limiter and certain other critical conditions were met.

A simulation[133] by Xu et al. of MARFE formation driven by an interplay of transport and radiation employed a series of edge simulations with the UEDGE 2-D fluid edge transport code[134] using a large input radial convection suggested by calculations from the BOUT boundary plasma turbulence simulation code.[135] The BOUT calculations for a DIII-D discharge indicated an increase of edge turbulence level (hence the associated radial transport) with collisionality (thus with radial location across the separatrix and into the SOL). These authors modeled the BOUT results in UEDGE by postulating a radial convective velocity that varied quadratically from 40 m/s at the separatrix to 300 m/s at the wall, over an outboard poloidal domain extending from the top of the plasma to 10 cm above the *x*-point. This outboard midplane radial convective transport was larger than the parallel transport toward the *x*-point. They found that with the reduced heat flux flowing toward the divertor, the flux tube expansion in passing near the *x*-point further significantly reduced the parallel heat flux relative to its upstream, midplane value. Such a reduction in heat flux led to a lower temperature near the *x*-point, hence via pressure conservation to a density and radiation buildup typical of a MARFE. While these authors were able to simulate the evolution of a MARFE-like state by a certain choice of transport parameters, they noted a strong sensitivity of the evolution of the MARFE-like state to the level of enhanced turbulent convective transport postulated near the midplane separatrix.

There have also been several investigations of the fundamental properties of the solutions of the coupled 2-D equations that govern MARFE formation. Meerson et al.[136] transformed these equations into a mixed Eulerian-Lagrangian framework, reducing the problem to a reaction-diffusion–type equation with nonlocality that obeyed length constancy and mass conservation along the magnetic field. Above a certain threshold level of radiative cooling, this model predicted the formation of MARFE-like condensations from a variety of initial conditions. Birk[137] developed a dispersion relation for condensation modes in a weakly ionized two-fluid hydrogen plasma in ionization equilibrium with a magnetic field. He found that the condensation and filamentation that are observed in astrophysical plasmas can develop on different timescales for the ionized and neutral components. Tokar[138] considered the MARFE as a special case of the dissipative structures that develop under critical conditions in different physical systems. Steele and Ibanez found several results that could be relevant to MARFEs in their investigations[139,140] of nonlinear 2-D thermal structures, in particular, that in many cases the nonlinear stability requirements are quite different from the linear stability requirements.

IV. DIVERTOR INSTABILITIES

Most stability analyses of the divertor region are based on a model such as is depicted in Fig. 6 and the set of 1-D Eqs. (21), (22), and (23). The SOL and divertor channel are represented as a long ribbon running along the field lines from some stagnation point to the divertor target plate. The width of the ribbon Δ may be determined by perpendicular transport considerations (in which case it may be different for energy and particles) or be fixed. Heat ($Q_\perp$) and particle ($\Gamma_\perp$) fluxes flow into the SOL from the core plasma, denoted in Eqs. (21) and (23) by the Heaviside function $H_\perp$, which is unity for $0 \le \xi \le L_\perp$. The Braginskii fluid equations are the ion particle continuity equation, with ionization source and recombination sink

$$\frac{\partial n}{\partial t} + \frac{\partial (nv)}{\partial \xi} = n(\nu_{ion} - \nu_{rec}) + \frac{\Gamma_\perp H_\perp}{\Delta_{nv}} \ , \qquad (21)$$

the combined ion and electron momentum balance equation

$$\frac{\partial (nmv)}{\partial t} + \frac{\partial}{\partial \xi}(2nT + nmv^2) = -nmv(\nu_{at} + \nu_{rec}) \ , \qquad (22)$$

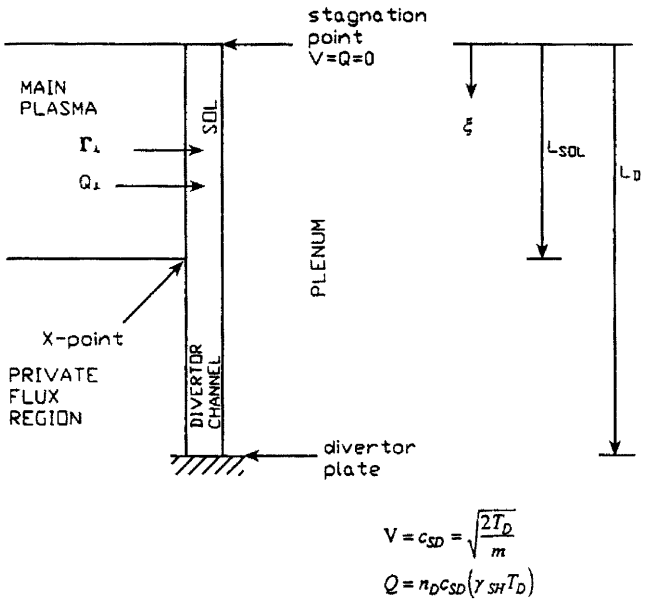

Fig. 6. One-dimensional model for particle, momentum, and energy transport along field lines in the SOL and divertor channel. (Stagnation boundary conditions at top, sheath boundary conditions at bottom.) Reprinted from Wiley-VCH with permission of Wiley-VCH.

and the combined ion and electron energy balance equation

$$\frac{\partial}{\partial t}\left(3nT+\frac{1}{2}nmv^2\right)-\frac{\partial}{\partial\xi}\left(\kappa_0 T^{5/2}\frac{\partial T}{\partial\xi}\right)+\frac{\partial}{\partial\xi}\left(\frac{1}{2}nmv^3+5nTv\right)=-n^2 f_z L_z-\frac{3}{2}nT\nu_{at}-nE\nu_{ion}+\frac{Q_\perp H_\perp}{\Delta_E}\ , \tag{23}$$

with the sheath and stagnation boundary conditions indicated in Fig. 6. Here, ν_{ion}, ν_{at}, and ν_{rec} are the ionization, combined charge-exchange plus elastic scattering, and recombination frequencies, and E_{ion} is the ionization energy.

IV.A. Radiative Detachment

Borrass[141] and Borrass et al.[142] used the above 1-D model of plasma particle, momentum, and energy flows along the field lines from the core-SOL interface to the divertor target, with sheath boundary conditions, coupled with a model for neutral recycling and impurity radiation in the divertor, to demonstrate that above a certain critical upstream density at the core-SOL interface, the solution becomes unstable, and the temperature in the divertor collapses. Since the model employs sheath boundary conditions, implying contact of the plasma with the divertor targets, the inability to obtain a solution perhaps should be interpreted as the plasma no longer being attached; i.e., the sheath boundary conditions are no longer valid. It should be noted that "partial detachment" frequently occurs in which the plasma and ion current near the separatrix are reduced to zero but remain finite farther away from the separatrix, but such a condition is difficult to treat in a 1-D model.

With reference to Fig. 6, the assumption that n, T, and v attenuate exponentially in the radial direction [e.g., $n(r)=n(0)\exp(-x/\Delta_n)$] and the continuity of radial particle and heat fluxes across the separatrix from the core into the SOL lead to the following width parameters:

$$\Delta_T=\frac{n_{\rm SOL}\chi_\perp T_{\rm SOL}}{Q_\perp(0)}\left(1+\frac{3D_\perp}{\chi_\perp}\frac{\Delta_T}{\Delta_n}\right)\ ,$$

$$\Delta_{n\nu}\equiv\frac{\Delta_n}{1+\dfrac{\Delta_n}{\Delta_\nu}}=\frac{n_{\rm SOL}\chi_\perp T_{\rm SOL}}{Q_\perp(0)(1+\Delta_n/\Delta_\nu)}\left(\frac{\Delta_n}{\Delta_T}+\frac{3D_\perp}{\chi_\perp}\right)\equiv n_{\rm SOL}\gamma_n\ , \tag{24}$$

and

$$\Delta_E\equiv\frac{2}{7}\Delta_T\qquad\Delta_{nT}\equiv\frac{\Delta_n}{1+\Delta_n/\Delta_T}\ ,$$

where $D_\perp$ and $\kappa_\perp$ are the perpendicular transport coefficients (usually assumed to be Bohm) in the SOL. Integrating Eqs. (21), (22), and (23) and the parallel conductive energy transport equation, $q=-\kappa_0 T^{5/2}dT/d\xi$, with the boundary conditions $n(\xi=0)=n_{\rm SOL}$, $n(\xi=L_{DIV})=n_D$ and $T(\xi=0)=T_{\rm SOL}$, $T(\xi=L_{DIV})=T_D$ leads to

$$n_D c_{SD}=\frac{\langle\Gamma_\perp\rangle L_{\rm SOL}}{\Delta_{n\nu}}+\Delta N_{at}\ , \tag{25}$$

$$T_D=\frac{1}{\gamma_{SH}}\frac{\langle Q_\perp\rangle}{\Gamma_\perp}\frac{\Delta_{n\nu}}{\Delta_E}\left[\frac{1-\dfrac{(\Delta Q_{rad}+\Delta Q_{at})}{\langle Q_\perp\rangle L_{\rm SOL}/\Delta_E}}{1+\dfrac{\Delta N_{at}}{\langle\Gamma_\perp\rangle L_{\rm SOL}/\Delta_{n\nu}}}\right]\ , \tag{26}$$

$$T_{\rm SOL}=\left[T_D^{7/2}+\frac{7}{2\kappa_0}\left\{\Delta Q_\perp\left(L_{DIV}-\frac{1}{2}L_{\rm SOL}\right)-(\Delta Q_{rad}+\Delta Q_{at})\frac{1}{2}L_{DIV}\right\}\right]^{2/7}\ , \tag{27}$$

and

$$n_{\rm SOL}=n_D\left[\frac{2T_D+\dfrac{1}{2}\dfrac{\Delta M_{at}}{n_D}\dfrac{\Delta_{n\nu}}{\Delta_{nT}}}{T_{\rm SOL}}\right]\equiv n_D K_{D\rm SOL}\ , \tag{28}$$

where

$\Delta Q_{rad},\Delta Q_{at}$ = integrals of the impurity radiation and the atomic physics power losses

ΔM_{at} = integral of the momentum exchange due to charge exchange, elastic scattering, and recombination

ΔN_{at} = integral of the net ionization particle source less recombination particle loss,

all over the interval $0\le\xi\le L_{DIV}$. Such attached divertor models have been extended by Stangeby,[143] Stacey,[144] Maingi et al.,[145] and Mahdavi et al.,[146] and the first two authors have shown the necessity of momentum exchange with recycling neutrals for detachment to occur.

Equations (24) through (28) must be solved numerically. Borrass[141] demonstrated that there is a minimum value of the temperature in front of the divertor target $T_D^{\rm min}$, below which the solutions are thermally unstable.

Since the solutions of these equations generally have an increasing n_{SOL} with a decreasing T_D, he identified the corresponding value of n_{SOL} as the limiting value of the upstream separatrix density for which an attached solution could be obtained:

$$n_{det} = n_{SOL}(T_D^{min}) = \frac{[9.1\kappa_0\pi^2\alpha^2]^{(m+2)/(7+m)}}{[g(32\pi^2)^2\gamma\beta^2a^4R^2]^{(9+2m)/(28+4m)}} \times \left(\frac{P_{sep}}{\chi}\right) q^{(1-2m)/(14+2m)} . \quad (29)$$

Borrass,[141] Borrass et al.,[142] Maingi et al.[145] and Mahdavi et al.,[146] give semiexplicit expressions for $n_{SOL}(n_D, T_D)$ obtained by substituting Eqs. (24) through (27) into Eq. (28) and making a few assumptions. These expressions exhibit a dependence on geometric parameters and the magnetic field that is useful for comparison of experimentally observed scalings, but these parameter dependences are very sensitive to the perpendicular transport assumptions that must be made to evaluate Eqs. (24).

The explicit form of Eq. (29) for the midplane separatrix density limit at detachment given by Mahdavi et al.[146] is used above, where κ_0 is the Spitzer thermal conductivity constant, γ is the sheath power transmission coefficient, $\beta = c_s/\sqrt{T}$, $\chi_\perp = \chi T^m$, P_{sep} is the power crossing the separatrix from the core, and α is an adjustable parameter. This expression has been shown to be capable, after normalization to other experimental data, of predicting the separatrix data at detachment for a series of DIII-D discharges, as shown in Fig. 7.

IV.B. Divertor MARFE

As mentioned previously, a sudden jump of a cool, high-density, radiating region from in front of the divertor target plate to a location upstream in the divertor plasma near the *x*-point is observed in diverted tokamak experiments. These "divertor MARFEs" have long been thought to be associated with thermal instabilities in the divertor plasma.

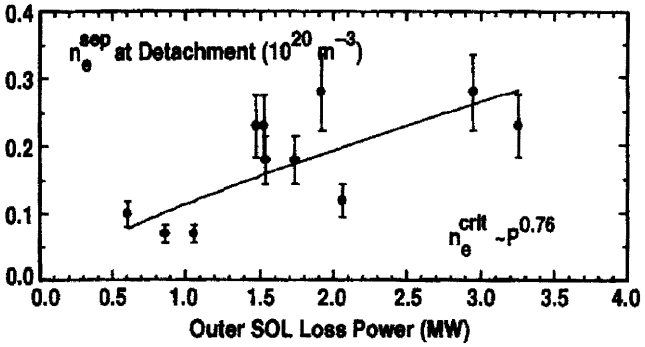

Fig. 7. Predicted and measured values of the electron density on the separatrix near the plasma midplane as a function of the power flux into the SOL for DIII-D shots.[146] Reprinted from American Institute of Physics with permission of American Institute of Physics.

Guided by the results of the DIII-D D_2 injection experiments,[147] in which divertor MARFEs appeared above a critical neutral pressure, and building on the previous modeling of divertor thermal instabilities by Capes et al.,[148,149] Ghendrih[150] investigated the divertor MARFE with a 1-D model similar to Eqs. (21), (22), and (23), but with separate ion and electron energy balance equations and neglecting recombination. Charge exchange with recycling neutrals was the dominant cross-field transport mechanism in the region between the ionization front (the location at which $T = 10$ eV in his model) and the divertor target. He found a bifurcation in the solution of the 1-D particle, momentum, and energy equations above a critical neutral density, at which the ionization front jumped from just in front of the target to 70% of the distance from the target to the *x*-point. In the region extending from the ionization front to the target plate, the plasma pressure dropped significantly. The control parameter determining the bifurcation point depended linearly on the neutral density, almost linearly on the distance along the field line from the *x*-point to the divertor target, but very weakly on the heat flux from the core into the SOL. These predictions of divertor MARFE formation were qualitatively confirmed by DIII-D experiments.[151]

Krasheninnikov et al.[152] considered essentially the same problem but with impurity radiation rather than charge exchange as the dominant cross-field loss mechanism. They found that reduction of the parallel heat flux into the recycling region (due to impurity radiation) below a critical value led to a bifurcation in the solution, leading to $T < 1$ eV in front of the divertor target and to a large drop in plasma pressure near the target. The mechanism causing the reduction in pressure was the interaction of the plasma with recycling neutrals. A further increase in radiation loss resulted in a rapid reduction in particle and heat fluxes to the target, i.e., to detachment. In a continuation of this work, Wising et al.[153] and Krasheninnikov et al.[154] established theoretically that volumetric recombination was important in the detachment process and that the location of the ionization front just in front of the target became unstable after detachment, causing a jump of the ionization front to upstream near the *x*-point, i.e., divertor MARFE formation.

Nakazawa et al.[155] examined the same problem of the stability of the radiation front in the divertor plasma with a 1-D plasma fluid-dynamics code, using equations similar to Eqs. (21), (22), and (23). They found that as the energy flux into the SOL from the core decreased, stable attached solutions evolved into stable detached solutions with the radiation front and the density peak located just in front of the divertor target, but as the energy flux decreased further, it became impossible to obtain a stable

detached solution with the radiation front located in the divertor. Instead, only dynamic solutions were obtained in which the radiation front moved upstream past the *x*-point into the SOL, leaving a cold, low-density plasma in the divertor channel. This unstable stage, in which the energy losses due to various atomic physics cooling mechanisms became larger than the input power into the divertor, occurred when the temperature in front of the divertor target dropped to a few electron volts and corresponds to the formation of a divertor MARFE.

Stacey[156] performed a linear stability analysis of the same 1-D SOL/divertor problem defined by Eqs. (21), (22), and (23), including both impurity radiation and recycling neutrals. Considering a temperature perturbation along the field lines in the divertor plasma of the form $\delta T'(\xi, t) = \delta T \exp(\omega t + i k_\parallel \xi)$, and similar expansions for the density and parallel velocity, he obtained a dispersion relation $\det[k_\parallel, \omega_{DIV}] = 0$ from the coupled density, momentum, and energy balance equations. The dispersion relation was quite complicated and had to be evaluated numerically. Analysis indicated that increasing heat flow into the SOL from the plasma, parallel heat conduction in the SOL and divertor, and volumetric recombination were stabilizing. On the other hand, increasing impurity radiation and atomic physics cooling in the SOL and divertor and increasing ion flux from the plasma into the SOL were destabilizing. Using experimental data, he evaluated the dispersion relation numerically to calculate the growth rate of parallel perturbations with scale lengths on the order of the length of the field lines in the divertor chamber, $k_\parallel^{-1} \approx L_{DIV} \sim q_{95}\pi R$, at several times during eight DIII-D discharges. The times at which the calculated growth rates changed from negative to positive were in good agreement with the times at which divertor MARFEs were observed to form in six of the discharges, as shown in Table I.

Krasheninnikov[157] and Krasheninnikov et al.[158] demonstrated that taking into account the 2-D V-shaped structure of the radiation front, which had a strong impact via perpendicular heat conduction on heat transport, enlarged the low-temperature (<10-eV) radiation region. The enlarged radiation region caused a larger radiative energy loss from the divertor plasma. For some conditions the transition to a V-shaped radiation front had a bifurcation character, such that the calculated radiation region jumped suddenly from the divertor target to near the *x*-point, suggestive of divertor MARFE formation.

IV.C. Heat Flux Asymmetry

The energy fluxes to the two divertor targets are generally found experimentally[159,160] to be asymmetric, both with single- and double-null divertors. While classical $E \times B$ and grad-B drift directions are in the correct direction to explain the asymmetries, thermal instability causes have also been put forward. Staebler[161] modeled the entire divertor and SOL from target plate to target plate (i.e., extended the divertor model of Fig. 6 to include another divertor leg and target plate at the top). He treated the divertor radiation as an addition to the usual sheath boundary condition at each target and found that if the divertor radiation increased with decreasing temperature, then there existed both a symmetric and an asymmetric solution for the heat fluxes to the two targets and that the symmetric solution became unstable above a certain radiation loss fraction, leading spontaneously to an asymmetric divertor heat flux condition. This critical radiation fraction (fraction of the heat into the divertor that was then radiated) above which the asymmetric heat flux solution appears was given by

$$f_{rad}^{\Omega sym} = (t_D^{1/2} + 3.5 t_D^{7/2})/[(1+2n)t_D^{1/2} + 3.5 t_D^{7/2}] \ , \tag{30}$$

where

$$t_D = T_D/[\, p(7L/16\kappa_0)2(4+k)/\{8m_i\}^{1/2}]^{1/3}$$

with

T_D = $(T_{D1}T_{D2})^{1/2}$ = mean value of the divertor temperatures at targets 1 and 2

p = pressure (assumed constant)

L = distance along field lines from target 1 to target 2

k = $\ln([m_i/4\pi m_e]^{1/2})$

n = parameter that characterized the temperature dependence of the radiation in the divertor $Q_{rad} \sim T^{-n}$.

Staebler[161] further noted that a difference in presheath temperatures between the two divertor targets would cause a difference in sheath potentials that would drive an "SOL current" from the hot to cold side, as previously suggested by Harbour et al.,[162] and that this current j would convect $-5/2Tj$ energy in the opposite direction in order to compensate for the higher power conducted to the hot side. Because of this SOL current, the critical radiation fraction at which the divertor heat flux solution becomes asymmetric is less than given by Eq. (30) when the divertor plates are grounded (the usual situation).

To model the effect of SOL currents on the divertor asymmetry, Hayashi et al.[163,164] and Shibata et al.[165] used essentially Eqs. (21), (22), and (23), without the charge-exchange, scattering, or recombination terms but with an additional $-d[(5/2+\alpha)jT/e]/d\xi$ energy convection term in Eq. (23), plus an Ohm's law equation

$$d\phi/d\xi = -\eta j + (\alpha/e)dT/d\xi \ , \tag{31}$$

a divergence-free current condition

$$dj/d\xi = 0 \ , \tag{32}$$

and the sheath boundary conditions

$$\Gamma_S = n_s\sqrt{\frac{2T_s}{m}} \ , \tag{33}$$

$$\frac{j}{e\Gamma_s} = 1 - \exp\left(\beta - \frac{e}{T_s}(\phi_s - \phi_p)\right) \ ,$$

$$q_s = \gamma_s \Gamma_s T_s \gamma_s \ ,$$

and

$$\gamma_s = \gamma_* - (2+\beta)\frac{j}{e\Gamma_s} - \left(1 - \frac{j}{e\Gamma_s}\right)\ln\left(1 - \frac{j}{e\Gamma_s}\right) \ ,$$

where

$\alpha = 0.71$

$\beta = 2.8$

$\gamma^* = 7.8$ for deuterium

$s, p =$ sheath entrance and the divertor plate, respectively.

They found that the SOL current causes a thermoelectric instability that destabilizes the symmetric divertor heat flux solution of the divertor/SOL plasma below a critical divertor plasma temperature at the sheath entrance,

$$T_{TE}^{asym} = T_s^{crit2} = (A/5)T_{\rm SOL} - (k/2\gamma^*)E_{ion} - (A/5)[T_{\rm SOL}^2 - (15kE_{ion}/A\gamma^*)T_{\rm SOL} + (5kE_{ion}/2A\gamma^*)^2]^{1/2} \ , \tag{34}$$

leading spontaneously to an asymmetric heat flux divertor solution, where

$A = [ae^2\eta * \kappa_0(L_{\rm SOL} + 2L_{DIV})r^{5/2}]/[14(\beta + 1 - \alpha)L_{DIV}]$

$r = T_{xpt}/T_{\rm SOL}$

$L_{\rm SOL} =$ total length along the field line from x-point to x-point

$L_{DIV} =$ length along field lines from the stagnation point to the divertor plate

$\eta = \eta * T^{-3/2} =$ plasma resistivity

$\kappa_e = \kappa_0 T^{5/2} =$ parallel electron heat conductivity

$k = P_{rad}/E_{ion} n \nu_{ion}$

$a =$ ratio of the resistivity averaged over the SOL and divertor to the value in the SOL.

This critical temperature for the thermoelectric instability to cause an asymmetric heat flux is found to be larger than the critical temperature below which the radiation-driven thermal instability would cause an asymmetric divertor solution in the absence of an SOL current:

$$T_{rad}^{asym} = T_s^{crit1} = kE_{ion}/\gamma^* \ . \tag{35}$$

V. TURBULENT TRANSPORT IN THE PLASMA EDGE

Investigations of the relation between turbulent transport and thermal instabilities in the plasma edge have been of two types. First, there have been investigations of edge turbulent transport produced by thermal instabilities, along the lines of the previously described thermal instability analyses for radial collapse of the temperature profiles, MARFEs, etc. Second, there have been investigations of changes in transport associated with electromagnetic turbulence that could produce thermal instabilities that caused dramatic transitions such as density limit disruptions, MARFEs, etc.

V.A. Turbulent Transport Caused by Thermal Instabilities

Stacey[166,167] has investigated the growth of short radial wavelength thermal instabilities in the edge pedestal that could cause transport enhancement. He expanded the densities, velocities, and temperatures about the equilibrium solutions in the form $T'(r, l_\perp, t) = T(r) + \delta T \exp(\omega t + i[k_\perp l_\perp + k_r r])$. Assuming that the radiative and atomic physics drive for thermal instabilities was localized in the edge pedestal, he considered perturbations with radial extent $k_r^{-1} \sim \Delta$ comparable to the edge pedestal width and perpendicular extent comparable to the poloidal circumference of the plasma. Substituting these equations into the 2-D particle, momentum, and energy balance equations, making use of the equilibrium solutions to constrain the equations for the perturbations and linearizing, led, to leading order, to a dispersion relation for the growth rates of thermal instability modes associated with ion and electron temperature instabilities of the form

$$\omega = -\frac{2}{3}\left(\chi(\nu L_T^{-2} + k_r^2) + \frac{5}{2}\nu\frac{\Gamma_\perp}{n}L_T^{-1} - \alpha\right) \ , \tag{36}$$

where the radiation and atomic physics terms differed for the ions

$$\alpha_i = \frac{5}{2}(\nu - 1)\nu_{ion} + \frac{3}{2}\nu_{at}^c\left(\nu - \left[1 + \frac{T_i}{\nu_{at}^c}\frac{\partial \nu_{at}^c}{\partial T_i}\right]\right) - \frac{1}{n}\left(\nu\frac{H_i}{T_i} - \frac{\partial H_i}{\partial T_i}\right) \tag{37}$$

and the electrons

$$\alpha_e = n_z\left(\frac{\nu L_z}{T_e} - \frac{\partial L_z}{\partial T_e}\right) + \nu_{ion}\left\{\frac{5}{2}(\nu-1) + \nu\frac{E_{ion}}{T_e} - \left(\frac{3}{2}+\frac{E_{ion}}{T_e}\right) \times \frac{T_e}{\nu_{ion}}\frac{\partial \nu_{ion}}{\partial T} - \frac{1}{n}\left(\nu\frac{H_e}{T_e} - \frac{\partial H_e}{\partial T_e}\right)\right\}, \quad (38)$$

where $\chi_r \sim T^\nu$ was used, $L_T^{-1} = -(dT/dr)/T$, and H is any external heating in the edge pedestal.

Assuming that the transport enhancement associated with these thermal instabilities can be represented by Kadomtsev's connection length expression $\Delta\chi \approx \omega k_r^{-2}$ (which implicitly assumes that the thermal instabilities drive fluctuating electric fields perpendicular to B to produce transport fluxes) and that the background transport in the absence of thermal instabilities is χ^0, the transport in the presence of thermal instabilities was represented as $\chi = \chi^0 + \omega k_r^{-2} H(\omega > 0)$, where $H(\omega > 0)$ is the Heaviside function, which is zero below the instability threshold $\omega = 0$ and unity above. Equation (36) was solved for the threshold value of L_T for which $\omega = 0$, and the radial heat conduction relation $q_r = Q_r - 5/2T\,\Gamma_r = nT\chi L_T^{-1}$ was used to convert this to a threshold condition for the total nonradiative radial power flux across the edge pedestal in terms of the radial ion flux Γ_r and the other quantities defined above:

$$\left(\frac{Q_r}{nT}\right)_{thresh} = \frac{5}{4}\frac{\Gamma_r}{n}\left[\sqrt{1 + \frac{(\chi^0(\alpha - \chi^0 k_r^2)/\nu)}{\frac{5}{4}\frac{\Gamma_r}{n}}} + 1\right]. \quad (39)$$

For nonradiative heat fluxes below the threshold value of Eq. (39), $H(\omega > 0) = 1$ and Eqs. (36), $\chi = \chi^0 + \omega k_r^{-2} H(\omega > 0)$ and the heat conduction relation $q_r = Q_r - 5/2T\,\Gamma_r = nT\chi L_T^{-1}$ can be combined to obtain a quadratic equation. The solutions plotted in Fig. 8 (for $\chi^0 = 10^3$ cm^2/s and $k_r^{-1} = 1.5$ cm) indicate that χ and L_T both decrease as the heat flux approaches the threshold and then drops sharply at the threshold.

The behavior shown in Fig. 8 is similar to what is observed at the L-H transition, which motivated Stacey and Petrie[168] and Stacey[169] to compare the predictions of Eq. (39) with the measured power crossing the separatrix ($P_{thresh} = A_{sep} Q_{thresh}$) at the L-H and H-L transitions in several DIII-D shots, where A_{sep} is the area of the separatrix. The sum of $P_{threshi}$ for the ions and $P_{threshe}$ for the electrons was compared with the measured power crossing the separatrix, P_{sep}^{exp} in Table II, for both L-H and H-L transitions in discharges with a wide range of edge conditions. Using a value $k_r^{-1} = 1$ cm, $\Delta\chi \approx \omega k_r^{-2}$ can exceed the representative H-mode thermal conductivity $\chi^0 \approx 0.1$ m^2/s for typical growth rates of $\omega > 10^3$/s. The particle flux across the separatrix was calculated from the plasma particle balance including recycling neutral and neutral beam injection. Clearly, there is agreement between the predicted power threshold of Eq. (39) and the measured power crossing the separatrix at the L-H and H-L transitions in these discharges, suggesting that the stabilization of $k_r^{-1} \approx 1$ cm thermal instabilities in the edge pedestal could be responsible for the L-H transition, and conversely that destabilization of $k_r^{-1} \approx 1$ cm thermal instabilities could be responsible for the H-L transition.

It is widely observed in H-mode experiments in which it is attempted to build up the density by continuous gas fueling (e.g., Refs. 170, 171, and 172) that the energy confinement time and the steepness of the edge pedestal density and temperature gradients all decrease with continued fueling. Stacey has suggested[173] that the destabilization and growth of short radial wavelength instabilities of the type discussed above, but with longer radial wavelengths that would cause a much less dramatic transport enhancement, could be responsible for the observed deterioration of χ and L_T^{-1} in the edge pedestal. Equations (36), (37), and (38) were evaluated[173,174] for the ion temperature instability growth rate at several times in some continuously gas-fueled DIII-D discharges in which the energy confinement times were observed to deteriorate with time. The calculations were made for $k_r^2 < \nu L_T^{-2}$ so that k_r^2 could be neglected in Eq. (36), which is not altogether consistent since the eikonal representation is not strictly valid when the temperature varies significantly over the wavelength of the perturbation. The increase with time of the calculated $\omega_i = \omega_{TB}$ and the decrease with time of the measured $H_{89P} = \tau_{exp}/\tau_{iter89p}$ (based on the ITER-89P scaling law) appeared to be correlated, as may be seen in Fig. 9.

V.B. Thermal Instabilities Caused by Changes in Electromagnetic Turbulent Transport

Turbulent transport in the edge pedestal and its relation to the L-H transition, confinement deterioration near the density limit, and the density limit itself have been an area of active research for a number of years, and the thermal instability theory summarized above is but one of many explanations that have been suggested. In fact, there is a far larger body of work on the role of electromagnetic-driven (MHD ballooning, electrostatic drift modes, etc.) turbulent transport. While a survey of electromagnetic turbulence theories is beyond the scope of this paper, a discussion of recent work relating changes in electromagnetic turbulence to density limits, confinement deterioration, and the L-H transition is appropriate. Recent surveys of earlier work on density limits[172] and the L-H transition[175] are available.

The leading paradigm for the improvement in confinement associated with a transition from L-mode to

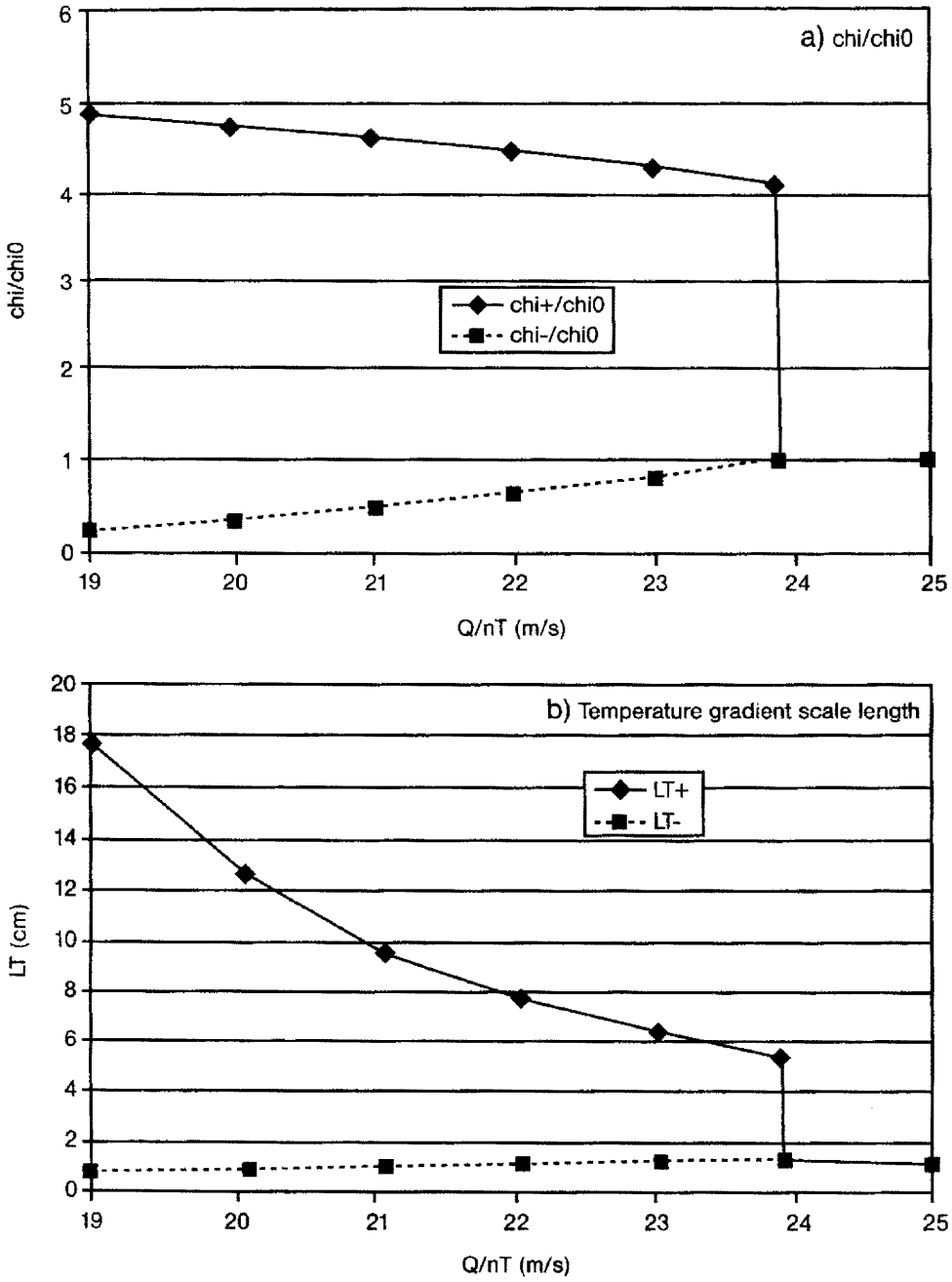

Fig. 8. Roots of (a) χ_i and (b) L_{Ti} as a function of the power flux through the plasma edge. [$\alpha_i = 5 \times 10^3$/s, $\chi_i^0 = 0.1$ m^2/s, and $k_r^{-1} = 1.5$ cm (Ref. 167).] Reprinted from Wiley-VCH with permission of Wiley-VCH.

H-mode is based on the creation of an edge boundary layer inside the LCFS, in which a strongly sheared flow suppresses turbulent fluctuations responsible for the poorly confined L-mode and causes the plasma to transition into the well-confined H-mode. A variety of mechanisms have been suggested that could generate sheared flow. The basic mechanisms for the generation of this flow and an associated radial electric field require either toroidal effects (e.g., ion-orbit loss or poloidally asymmetric transport driven by Stringer spinup) or the generalized Reynold's stress of the turbulent waves responsible for the "anomalous" L-mode transport, which waves become unstable to the generation of the sheared flow. (Note that suppression of thermal instabilities is also predicted[166] to generate sheared flow.) However, at present there is no direct experimental confirmation that "zonal" flow driven by plasma turbulence is the mechanism causing the observed L-H transition.

TABLE II

Some DIII-D Shots just Prior to the L-H or H-L Transition*

Shot Number	Time (ms)	I (MA)	B (T)	P_{NB} (MW)	n_{eped} (10^{19}/m^3)	T_{eped} (eV)	P_{sep}^{exp} (MW)	P_{thr} (MW)
L-H								
102456	1725	1.4	2.0	2.6	3.22	95	1.55 to 1.86	1.54
97979	1900	1.4	2.0	2.0	2.59	125	1.72 to 2.04	2.18
92079	2275	1.0	2.1	6.8	1.28	220	3.99 to 4.06	4.00
84027	2575	1.3	2.1	1.1	2.94	144	1.28 to 1.36	1.13
H-mode								
97979[a]	3250	1.4	2.0	6.5	6.35	525	4.64 to 4.96	2.59
H-L								
92976	3210	1.0	2.1	5.0	4.95	275	3.96 to 4.33	4.21
101565	4950	1.4	2.0	4.7	6.75	170	4.21 to 4.85	4.60
102456	3500	1.4	2.0	2.4	6.25	150	2.48 to 2.82	2.36
102461	3300	1.4	1.5	2.4	7.80	170	2.11 to 2.17	2.18

*R = 1.71 to 1.79 m, a = 0.6 m, κ = 1.73 to 1.89, LSN divertor, $\chi^0 = 0.1$ m^2/s, $k_r^{-1} = 1$ cm (Refs. 167 and 168).
[a]Well into H-mode phase, not at the L-H of H-L transition—control case.

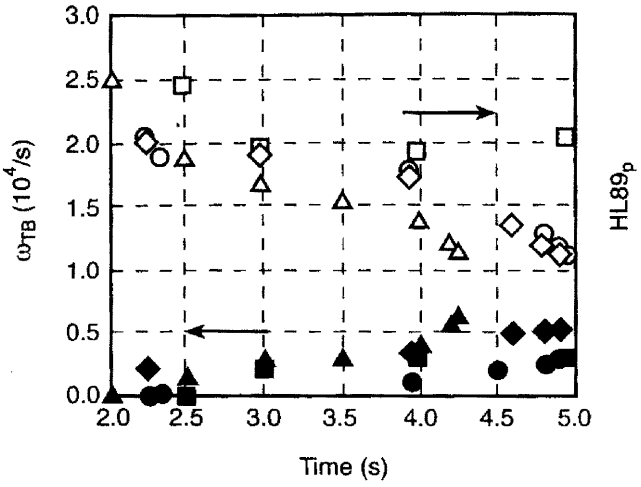

Fig. 9. Correlation between decreasing energy confinement time (empty symbols—HL89p, the confinement multiplier relative to the ITER-89p scaling law) and the ion temperature edge thermal instability growth rate [$\omega_{TB} = \omega_i$ of Eq. (36)] (Ref. 174). Reprinted from Wiley-VCH with permission of Wiley-VCH.

At the most sophisticated level, fully 3-D fluid simulation codes that provide first-principle modeling of the edge turbulence and anomalous transport and their interplay with self-generated or imposed shear flows have been developed. Rogers et al.[176] carried out 3-D Braginskii transport simulations in a poloidally and radially localized edge region flux tube that wound around the torus and showed that the level of turbulent transport could be related to two parameters: a normalized pressure gradient "ballooning" parameter

$$\alpha = -Rq^2 d\beta/dr \tag{40}$$

and a diamagnetic parameter

$$\alpha_d = \left(\rho_s c_s \left(\frac{RL_n}{2}\right)^{1/2}\right) \Big/ \left(\left[1 + \frac{T_{i0}}{T_{e0}}\right] L_n L_0\right) , \tag{41}$$

where

L_n = density gradient scale length

$$L_0 = (2\pi q_a R)\left[\frac{(C^2\eta_{\|})}{4\pi v_A^2 (Rq^2/2)}\right]^{1/2}$$

C = geometric function

v_A = Alvfén speed

ρ_s = gyroradius

c_s = ion sound speed.

For small α_d the calculated turbulence resulted mainly from the nonlinear development of resistive ballooning modes, and at very small α_d the calculated ion radial energy flux became very large (inferred transport coefficients $\approx$ 60 m^2/s), a result that was argued to be consistent with an effective density limit above which stable operation is impossible and with the observed confinement deterioration as the density limit is approached. For $\alpha_d \approx 1$ the turbulent transport was predicted to be primarily due to nonlinear electron drift waves, with small increases in pressure gradients (α) leading to a strong

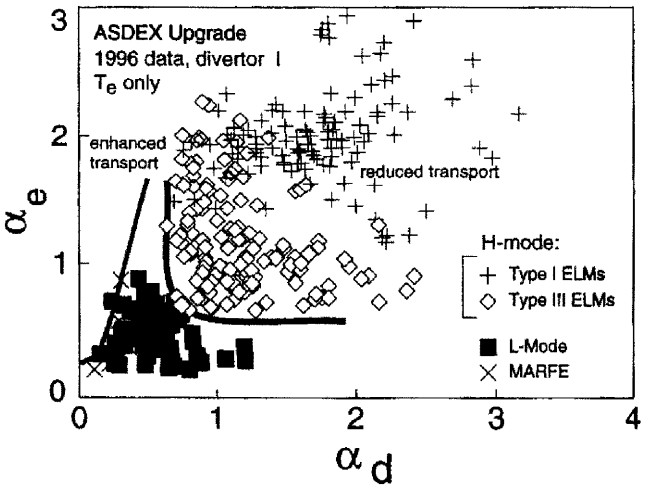

Fig. 10. Plasma operating regimes in edge plasma phase-space.[172] Reprinted from Wiley-VCH with permission of Wiley-VCH.

suppression of transport, which would further increase the pressure gradient and lead to the spontaneous formation of a transport barrier (i.e., the L-H transition) above a certain threshold value of α. These considerations indicate that the different regimes of plasma operation in the phase-space spanned by α and α_d might look like Fig. 10.

Guided by these results, Guzdar et al.[177] developed a theory for the generation of zonal flow (ϕ_s, the scalar potential) and field ($A_{\|s}$, the vector potential) by finite-β drift waves that indicated that the important parameter that determines the growth rate of the zonal flow and field is $\hat{\beta} = \frac{1}{2}\beta(qR/L_n)^2$. The growth rate for zonal flows has a minimum at $\hat{\beta}_c$, which was identified as the L-H threshold, corresponding to the threshold

$$\Theta_c \equiv (T_e/\sqrt{L_n})_{thresh} = 0.45 B^{2/3} Z_{eff}^{1/3}/(RA_i)^{1/6} \quad . \quad (42)$$

Comparison[178] with several DIII-D L-H transitions showed that the measured values of the parameter $\Theta \equiv (T_e/\sqrt{L_n})$ underwent a sharp increase from below to above the threshold value at the time of the L-H transition, as shown in Fig. 11, and that a sharp decrease in L_n preceded the increase in T_e. We recall that the thermal instability theory for the L-H transition is based on a sharp decrease in L_T, caused by the suppression of thermal instabilities, at the L-H transition. Clearly, it would be interesting to extend thermal instability theory to include the particle balance equation to determine if L_n would enter an extended thermal instability L-H threshold theory, to determine if L_T would enter an extended finite-β drift wave theory, and then to compare the two against experimental data.

Xu et al.[133] carried out a series of 3-D BOUT simulations[135] for a DIII-D model problem that found that turbulent fluctuations and the associated radial transport in the plasma edge and SOL increased with collisionality. At high density, the radial turbulent transport dominated the classical parallel transport in the SOL, leading to destruction of the edge shear layer and extension of the region of high radial transport inside the separatrix. As the density was increased, these simulations showed evidence of the formation of a resistive x-point mode, then of a resistive ballooning mode, and then of detachment from the divertor. The anomalous transport coefficient inferred from the drift resistive ballooning (DRB) mode turbulent fluxes rose to 10 to 30 m^2/s toward the end of the simulation, which was interpreted as a density limit. Associated 2-D UEDGE fluid edge plasma calculations[134] with suitably chosen large radial convection terms and other transport coefficients then predicted the formation of MARFE-like structures at the x-point (as discussed in Sec. III.I), which were interpreted as representing the density limit. These simulations suggest an explanation of density limits in terms of the dependence of turbulent transport on collisionality and the interplay with radiation but did not provide quantitative predictions of a density limit that could be compared with experiment.

Tokar et al.[179,180] have proposed a similar explanation for the density limit in terms of the interplay of turbulent transport and radiation. They argue that with increasing density and decreasing temperature, the DRB modes with transport coefficients scaling as $D_{\mathrm{DRB}} \sim n/\sqrt{T}$ should become dominant in the edge, producing a drastic increase in particle and energy loss and reduction of edge temperature, thus causing a strong increase in edge impurity radiation. A thermal equilibrium of the edge power balance is argued not to exist above a certain maximum edge density that is very close to the edge density at which the DRB mode transport becomes dominant:

$$n_{\mathrm{DRB}} \sim q_{core}^{0.24} \frac{I^{0.6}}{B^{0.12}} \quad . \quad (43)$$

They noted the correspondence of expression (43) to the Greenwald density limit scaling for ohmic heating where the power flux out of the core into the edge $q_{core} \sim I$.

VI. DENSITY LIMITS

Threshold conditions for the onset of various thermal instabilities have been identified in Secs. II through V. These threshold conditions involve the physical parameters that act to stabilize and destabilize the instability and constitute explicit or implicit limits on the particular density involved in the specific thermal balance (i.e., the density in the edge, in the divertor, averaged over the core) for the instability of which determines the onset of the respective thermal instability. In contrast,

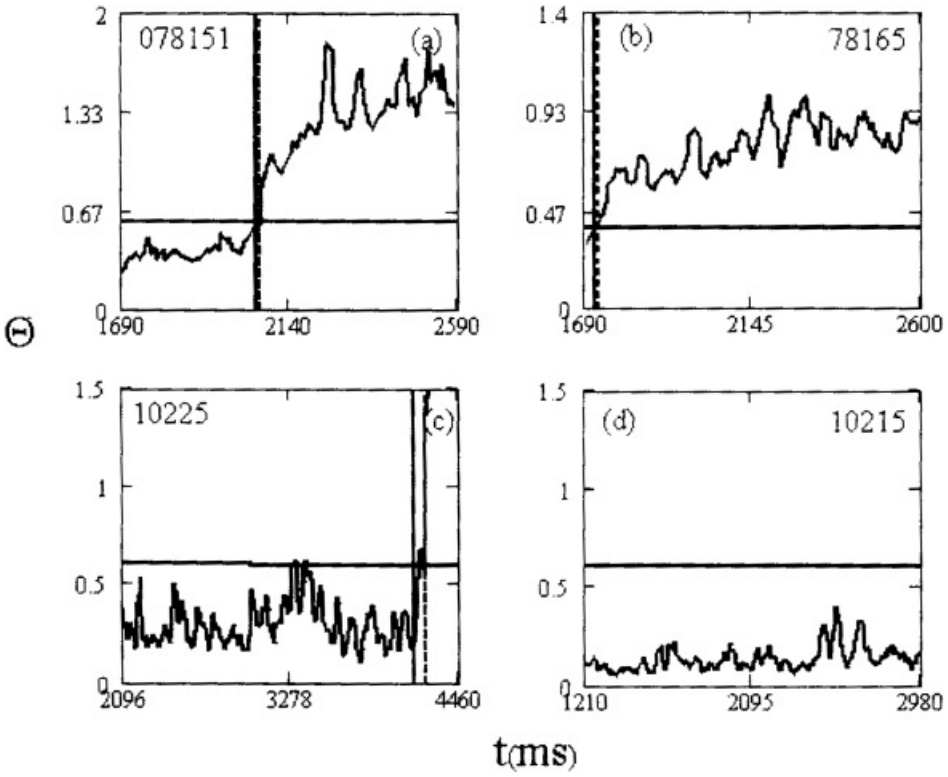

Fig. 11. The quantity $\Theta = T_e / \sqrt{L_n}$ versus time for four DIII-D discharges, the first three [(a), (b), and (c)] of which underwent an L-H transition. Θ_c of Eq. (42) is plotted as solid horizontal line. Vertical solid line indicates last L-mode data point, and vertical dashed line is first H-mode data point.[178] Reprinted from American Institute of Physics with permission of American Institute of Physics.

experimental density limits tend to relate readily measured or otherwise known quantities, e.g., to correlate the line average density with magnetic field, plasma current and size, etc.

Another difficulty encountered in relating a thermal instability onset density with an experimental density limit is that the terminology used in discussing density limits varies considerably. Some authors use "density limit" to mean the density limit for disruption, and other authors use it to mean the maximum achievable density no matter how limited (e.g., fueling limitation, confinement deterioration, MARFE formation).

VI.A. Disruption

The first disruption density limit apparent from the early tokamak experimental data seems to have been the Murakami limit[181] relating the line average electron density to the ratio of the toroidal magnetic field to the major radius, $n_e = MB_t/R$, where the Murakami number M varied with input power and impurity content. A second trend that was found in the early data was that the maximum line-averaged density scaled with the plasma current, which gave rise to the Hugill[182] plot of $M = n_e R/B_t$ versus $1/q_a$ as the way of characterizing the disruption density limit data for a given machine, an example of which is shown in Fig. 12. In searching for a commonality among the characterization of the disruption density limit data from Alcator C, DIII, and Princeton Beta Experiment (PBX), Greenwald et al.[183] found that the simple scaling $n_e = I/\pi a^2$ characterized the maximum line average electron densities achieved in these three machines with different currents, fields, plasma radii, and elongations. This "Greenwald density," $n_{GW} = I/\pi a^2$, has been found to approximately characterize the disruption density limit in many subsequent experiments, including those with auxiliary heating, although there are many examples of machines that can only achieve densities a fraction of n_{GW} and several examples[184–187] of discharges with densities that exceed n_{GW} by up to a factor of 2. An extensive survey of the experimental evidence related to the density limit is given in Ref. 188.

The present understanding of a disruption is in terms of destabilization of the $m = 2$ MHD tearing mode by a negative current gradient inside the resonant $q = 2$ surface and particularly by a negative current gradient close to the resonance surface. With respect to Fig. 12, the low-q disruptions are thought to be caused by the $q = 2$

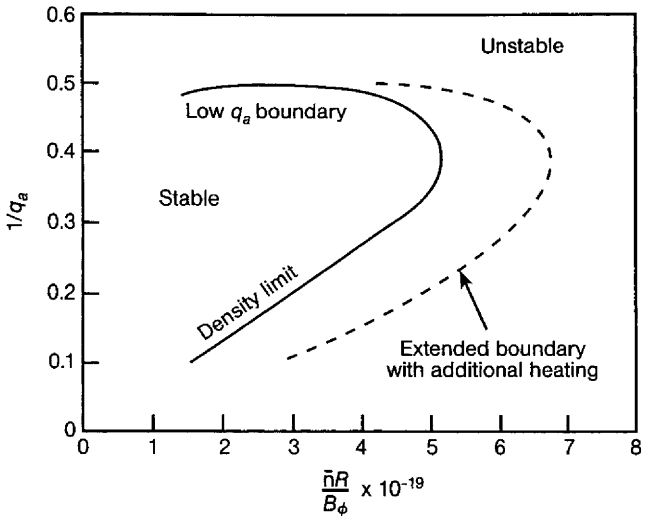

Fig. 12. Typical Hugill diagram of the disruption operational boundary in a tokamak.[189] Reprinted from Wiley-VCH with permission of Wiley-VCH.

surface moving outward into the region of sharp negative current gradient with increasing plasma current, triggering the $m = 2$ tearing mode. The low-q disruption limit is essentially a current limit on tokamak operation, and thermal instabilities are not involved in any significant way.

On the other hand, the higher-q disruptions are thought to be caused by the radial collapse of the current channel moving the region of steep negative current gradient inward to the location of the $q = 2$ surface and thereby destabilizing the $m = 2$ tearing mode. The radial collapse of the current channel in turn is caused by the inward collapse of the radial temperature profile driven by the radiative thermal instability discussed in Sec. II, so the thermal instability critical densities for radiative collapse of the radial temperature profile summarized in Sec. II may be used as surrogates for higher-q disruption density limits. It should be noted that most of the density limits cited in Sec. II were limits on the edge density, although the density limits of Eqs. (1) and (2) should be interpreted as core average densities.

Quantitative comparison of the radiative collapse density limit predictions with experimental data has been limited. The radiative collapse density limit prediction of Eq. (2) was evaluated by Stacey and Petrie[13] at several times over the course of two DIII-D shots (90323, 93796) in which pellet injection was used to achieve densities well in excess of n_{GW} before terminating in disruptions. The measured line average densities exceeded the radiative collapse density limit of Eq. (2) well before the disruption, in both shots, and there was experimental evidence of radiative collapse at these times. Kelly et al.[190] simplified Eq. (2) and demonstrated that the parameter scaling was consistent with the empirical parameter scaling of the disruption density limit found experimentally in TEXTOR, and Stacey[11] showed that Eq. (2) reduced to the Greenwald scaling $n \sim I/\pi a^2$ for ohmic-heated plasmas.

VI.B. Detachment

The detachment density limits, e.g., Eqs. (20) and (29), are limits on SOL density at the plasma midplane in limited and diverted tokamaks, respectively. The detachment limit of Eq. (29) has been taken as a surrogate for a disruption limit[141,142] in ASDEX, on the strength of the observation that detachment always resulted in disruptions in ASDEX. Taking the ratio of the separatrix density to the line average density and certain other model parameters from experiment, the detachment density limit calculated with Eq. (39) of Ref. 141—equivalent of Eq. (29)—was compared with the measured disruption density limit in a series of L-mode discharges in ASDEX, and the agreement shown in Fig. 13 was quite good.

It should be noted that while the detachment density limit is a useful surrogate for the disruption density limit in ASDEX and some other experiments, this is not always the case. For example, TFTR could operate stably in the detached condition with good confinement[84,89]; JET ELMy H-mode discharges operated stably after detachment, although beyond certain levels of continued gas fueling the density was limited by confinement deterioration[191]; and continuously gas-fueled DIII-D H-mode discharges evolved through divertor MARFE formation and x-point core MARFE formation before the density was finally confinement limited by an H-L transition.[92–95] The explicit result for Eq. (29) obtained by Mahdavi et al.[146] was shown to predict the midplane separatrix density at detachment in several DIII-D discharges, after normalization to experimental data.

Even when not a good surrogate for the disruption density limit, the detachment density limit has value in

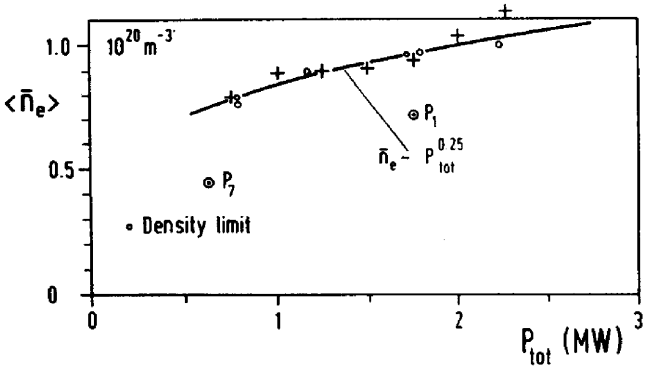

Fig. 13. Calculated (+, o) maximum separatrix density at midplane times an experimental determined $\langle n_e \rangle / n_{sep}$ compared with fit of measured (curve) values of $\langle n_e \rangle$ at disruption in ASDEX (Ref. 141). Reprinted from *Nuclear Fusion* with permission of *Nuclear Fusion*.

its own right since it sets the maximum value of the density at the midplane separatrix, which is an important element in the determination of the core density.[146]

VI.C. MARFEs

Since MARFEs radiating copiously inside the separatrix invariably cause a back transition from H-mode to L-mode (apparently by reducing the nonradiative power crossing the separatrix and increasing the power that is required to stay in H-mode[192]) in DIII-D (Refs. 92 through 95) and ASDEX-U (Ref. 96), the MARFE onset edge density threshold can serve as a surrogate for a confinement deterioration to the L-mode density limit. In TEXTOR, a MARFE is usually followed by disruption,[63] allowing the MARFE onset edge density limit to serve as a surrogate for a disruption density limit. As discussed in Sec. III, the MARFE threshold edge density expression of Eq. (19) has been successful in predicting the formation of MARFEs in several discharges in DIII-D and TEXTOR.

VI.D. Confinement Deterioration

In many shots with continuous gas fueling, the density first increases and then saturates or even decreases after a certain time because of a decrease in confinement. As discussed in Sec. V, one possibility for the decrease in confinement is the growth of thermal instabilities with short radial wavelengths in the edge plasma inside the separatrix,[173] which could increase the edge transport. A second possibility is the change in the nature of the electromagnetic turbulent transport with increasing density,[176] and a third is the interaction of thermal instabilities and edge turbulence.[180]

As an example,[174] the line average density in DIII-D shot 97979 was saturated at $\sim 0.8 \times 10^{20}/\mathrm{m}^3$ between 3.0 and 3.75 s and then increased after 3.75 s, as shown in Fig. 14, even though gas fueling continued at $\sim$57 Torr·l/s throughout the entire period. The measured τ_E^{exp} decreased from 3.0 to 3.75 s, offsetting the continued fueling, and then was constant, allowing the continued fueling to build up the density after 3.75 s. The calculated growth rate of the ion temperature thermal instability given by Eq. (36) (and the somewhat smaller growth rate of the electron temperature instability) increased sharply over the same period, 3.0 to 3.75 s, that the confinement time decreased and then increased only slowly thereafter, exhibiting a strong correlation with the measured confinement time.

VII. THERMAL INSTABILITY ANATOMY OF A DISCHARGE

It is useful to consider the experimental evidence for and theoretical interpretation of thermal instabilities in detail. Several abrupt transitions that can be understood as thermal instabilities are manifest in the diagnostic traces

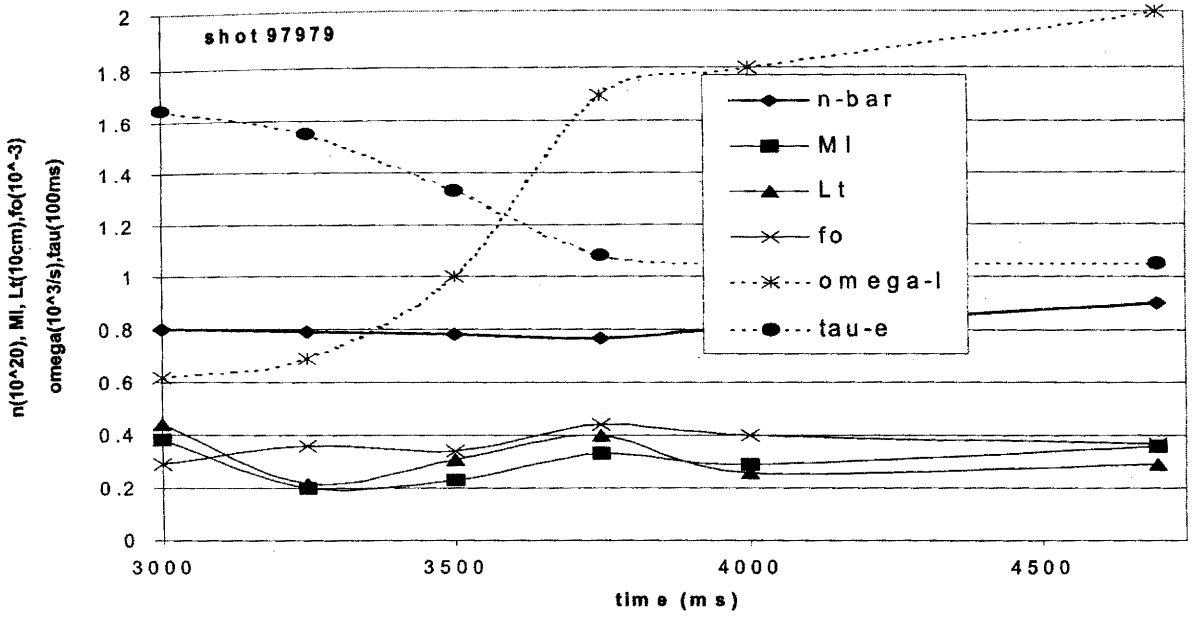

Fig. 14. Calculated and measured density limit phenomena in DIII-D shot 97979 (n-bar = experimental line average density; tau-e = experimental energy confinement time; omega-i = thermal ion temperature instability growth rate ω_i of Eq. (36); Lt = ion temperature gradient scale length L_T; MI = ratio of experimental edge density to theoretical threshold density for MARFE onset of Eq. (19); fo = calculated average neutral concentration in edge).[174] Reprinted from American Institute of Physics with permission of American Institute of Physics.

shown in Fig. 15 for a heavily gas-puffed H-mode discharge in DIII-D. This shot was continuously gas fueled from 2.0 to 3.5 s and again from ~3.8 to 4.5 s (Fig. 15a). The density initially rose when the gas fueling began (Fig. 15b), and the power radiated from the core and the SOL and upper divertor plasma near the *x*-point increased accordingly (Fig. 15c).

The plasma detached from the outer divertor target at ~2800 ms, as indicated by probe current data near the separatrix strike point in Fig. 15d. Promptly thereafter a divertor MARFE formed in the vicinity of the *x*-point but outside the separatrix over 2962 to 3000 ms, as indicated by the Thomson scattering measurements of n_e and T_e (Figs. 15e and 15f) for a location just outside of the separatrix near the *x*-point in the divertor plasma, and by the bolometer data from a chord through the same location (Fig. 15g). The sharp increase in density and decrease in temperature at this location and the measured increase in radiation along a chord passing through this location are indicative of the formation a highly radiating, dense, cool region (divertor MARFE) just outside the separatrix near the *x*-point. The theoretical growth rate for divertor thermal instabilities leading to a divertor MARFE (calculated by solving the dispersion relation formed from Eqs. (12), (13), and (14) of Ref. 156 and discussed in Sec. VI), ω_{DIV}, was calculated to be strongly negative (stable against divertor MARFE formation) at 2700 ms but to become positive (unstable) by 3000 ms, as indicated in Table III, indicating a prediction of divertor MARFE formation in this time interval, probably more toward the end than the beginning. This prediction is consistent with the experimental data.

The measured energy confinement time decreased, and the measured D_α signal (inversely related to particle confinement) increased after ~2000 ms, as shown in Figs. 15h and 15i. The calculated growth rates from

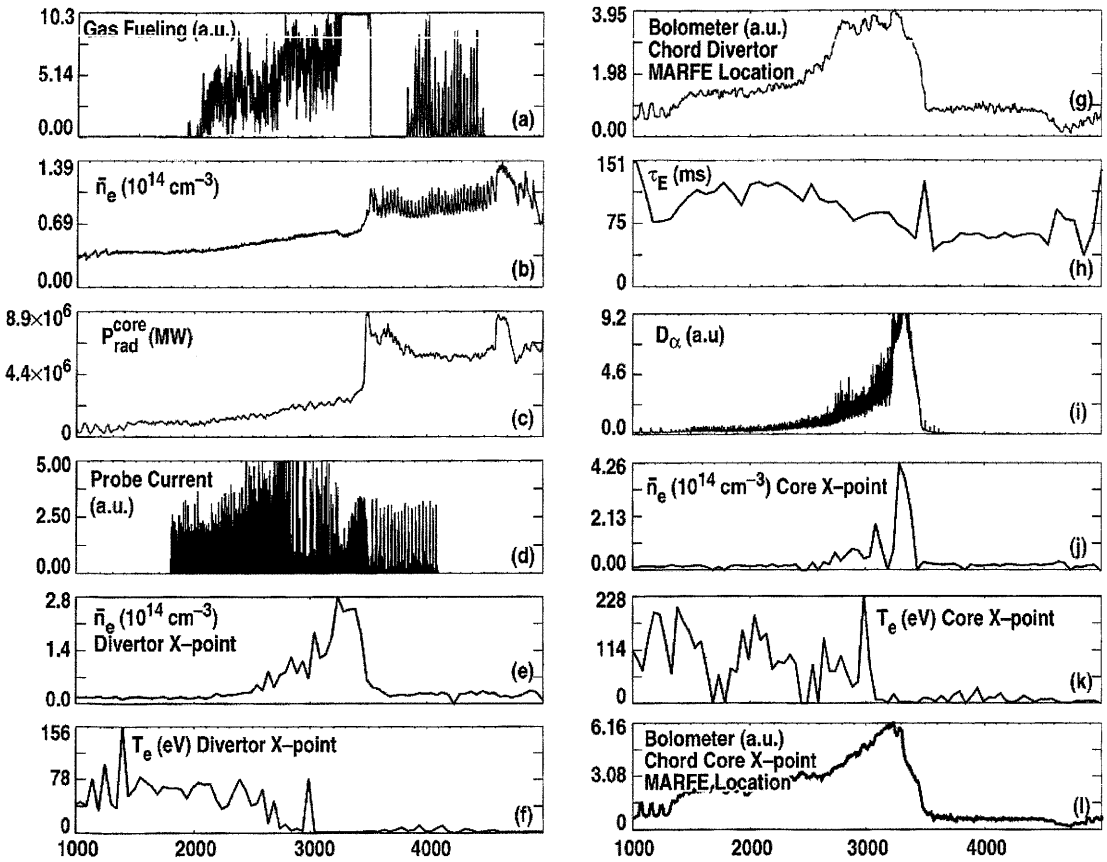

Fig. 15. Manifestations of thermal instabilities in gas-fueled DIII-D discharge 92976: (a) gas injection rate; (b) line-average density; (c) radiative power exclusive of divertor chamber; (d) probe signal at the outer divertor separatrix strike point; (e) Thomson scattering n_e at location in divertor plasma just outboard of *x*-point; (f) Thomson scattering T_e at location in divertor plasma just outboard of *x*-point; (g) bolometer signal from chord through location in divertor plasma just outboard of *x*-point; (h) energy confinement time; (i) D_α through *x*-point; (j) Thomson scattering n_e at location in core just above *x*-point; (k) Thomson scattering T_e at location in core just above *x*-point; (l) bolometer signal from chord through location in core just above *x*-point.

TABLE III

Thermal Instability Parameters for DIII-D Shot 92976*

	Time (ms)								
	2500	2700		3000		3312		4500	
n_{ped} (10^{20} m^{-3})	0.41	0.51		0.48		0.47			
T_{eped} (eV)	346	343	D	237	C	187	H		D
ω_{DIV} (10^5/s)	−25.2	**−24.8**	I	**6.5**[a]	O	22.4	—		I
ω_{iTB} (10^4/s)	0.09	0.27	V	0.44	R	0.69	L		S
L_{Ti} (cm)	3.1	5.0		5.1	E	5.4			R
S_{recyc} (10^{20}/s)	1.31	1.41		1.95		6.95			U
$MI = n_{\exp}/n_{\text{MARFE}}$	0.20	0.41		**0.63**		**1.38**[b]	T		P
$P_{radcore}$ (MW)	0.54	0.42	M	0.39	M	1.37	R		T
$P_{sep}^{\exp}$ (MW)	4.67	4.85	A	4.56	A	**4.14**[c]	A		I
P_{thresh} (MW)	2.68	3.11	R	3.19	R	**3.97**	N		O
$(\Gamma/n)_{sep}$ (m/s)	12.2	16.2	F	21.7	F	25.1	S		N
α_i (10^3 s^{-1})	0.51	0.47	E	0.84	E	1.49			
α_e (10^3 s^{-1})	0.71	0.63		1.20		2.04			
$DI = n_{\exp}/n_{disrup}$	0.40	0.40		0.69		**0.84**		**1.08**	

*Reference 92. $P_{nb} = 5$ MW, $q_{95} \approx 6$, $B = 2.1$ T, $I = 1.0$ MA, $R = 1.7$ m, $a = 0.6$ m, $\kappa = 1.8$, LSN.
[a]The divertor MARFE formed 2962 to 3000 ms experimental.
[b]The *x*-point MARFE formed 3050 to 3100 ms experimental.
[c]H-L transition at 3230 ms experimental.

Eq. (36), ω_{iTB}, of ion temperature thermal instabilities with radial wavelengths $k_r^{-1} < \sqrt{\chi^0/\omega}$ in the edge pedestal that are discussed in Sec. V increased with time after 2000 ms, as shown in Table III. (Figure 9 shows the increasing calculated ω_{iTB} and the decreasing measured confinement [H_{89}] for several similar shots.) This increase in ω_{iTB} was estimated to increase the edge ion thermal transport rate as $\Delta\chi_i \approx \omega_{iTB} k_r^2 \approx (10^3 \text{ to } 10^4)$ $k_r^2 \sim 400$ to 4000 cm^2/s for $k_r^{-1} \approx 0.5$ cm. Relative to typical values of $\chi_i \approx 1000$ cm^2/s in H-mode edge transport barriers, this increase in the transport rate is the same order as the observed decrease in confinement shown in Fig. 15h. The measured ion temperature gradient scale lengths L_{Ti} in the edge increased with time after 2000 ms, as shown in Table III, implying an increase in the edge χ_i. A similar result was found for ω_{eTB} and L_{Te}. This correlation between the measured decrease in particle and energy confinement and the predicted increase in the edge transport rate due to thermal instabilities is suggestive of a cause-effect relation.

With continuous fueling, the plasma and particularly the neutral densities in the edge (inside the separatrix) built up, as indicated in Table III by n_{ped} and the quantity S_{recyl}, which is the source rate of neutrals (from the instantaneous gas injection and from the recycling of plasma ions from the divertor plate) that are crossing inward across the separatrix into the edge plasma. After sufficient neutral buildup in the edge pedestal, an *x*-point MARFE formed between (3050 and 3100 ms), as indicated by the Thomson scattering measurements of n_e and T_e shown in Figs. 15j and 15k for a location inside the separatrix above and outboard of the *x*-point, and as indicated by the bolometer data shown in Fig. 15l for a chord passing through the core region just above the *x*-point. The ratio MI of the experimental edge density in the pedestal region to the predicted threshold density for MARFE formation given by Eq. (19) increased from below to above unity, predicting core *x*-point MARFE formation, sometime between 3000 and 3312 ms, as shown in Table III, consistent with the experimental observation.

A back H-L transition took place at 3230 ms, as indicated by the increase in the D_α signal from a chord through the *x*-point shown in Fig. 15i. The ratio of the predicted threshold power crossing the separatrix needed to stabilize $k_r^{-1} \approx 1$ cm thermal instabilities given by Eq. (39) to the measured power crossing the separatrix increased from well below unity at 2500 ms to about unity at 3212 ms just before the measured H-L transition at 3230 ms, as shown in Table III. The radiative power from inside the separatrix ($P_{radcore}$) increased as a result of the core MARFE, significantly reducing the nonradiative power flowing outward across the separatrix ($P_{sep}^{\exp}$) after the formation of the core MARFE. During the same time, the H-L power threshold (P_{thresh}) of Eq. (39) was increased even more significantly because of the increase of the radial particle velocity $V_{rsep} = (\Gamma/n)_{sep}$ caused by the ionization of the increased neutral influx (S_{recyl}) that accompanied core *x*-point MARFE formation and because of the increase of the atomic physics cooling parameters α_i and α_e given by Eqs. (37) and (38) due to

the increased neutral influx. The fact that the nonradiative power crossing the separatrix at 3312 ms was essentially the same as the predicted H-L threshold power indicates that an H-L transition is predicted to take place, which it does very shortly thereafter. Values of the background transport ($\chi_0 = 10^3$ cm^2/s), perturbation wavelength ($k_r^{-1} \approx 1$ cm), and temperature dependence ($\chi_0 \sim T^\nu$, $\nu = 2.5$) were used in these calculations, but studies indicated a weak sensitivity to small variations in these values.

The divertor MARFE and core *x*-point MARFE coalesced into a core MARFE after ~3450 ms and rotated rapidly inboard and upward, as indicated by bolometer chords passing through the divertor MARFE (Fig. 15g) and core *x*-point MARFE (Fig. 15l) locations and by bolometer chords passing through higher inboard locations (not shown), to form a core MARFE inside the separatrix at the top of the plasma at ~200 to 240 deg (measured clockwise from the outboard midplane) by ~3467 ms.

As indicated by the probe data in Fig. 15d (and by data from other probe locations), the plasma completely detached from the outer divertor plate at ~3478 ms, at which time the plasma density and radiation increased sharply, as shown in Figs. 15b and 15c. At this event, the feedback-controlled gas fueling was temporarily terminated, as shown in Fig. 15a.

The ratio *DI* of the plasma line average density to the density n_{rc} predicted by Eq. (2) at which the plasma becomes thermally unstable to radiative collapse of the temperature and density profiles is below unity through 3212 ms but becomes slightly greater than unity by 4500 ms, predicting that a radiative collapse was underway by that time. A thermal collapse of the temperature profile through the $q = 2$ mode location would be expected to trigger an $m = 2$ mode and lead to a disruption. A locked mode was observed to start to grow at 4770 ms and to reach a saturated phase by 4920 ms, which lasted until 4995 ms, at which point diagnostic information ceased to be available.

VIII. FUSION INSTABILITIES

VIII.A. Instability Analysis

It was first recognized by Mills[1] that the strong positive temperature dependence of the D-T fusion cross section $\langle\sigma v\rangle \sim T^2$ in the 10-keV range would destabilize the global power balance in a fusion reactor

$$dU/dt = (P_\alpha + P_{aux}) - (P_{rad} + P_{tran}) \ , \qquad (44)$$

where

U = thermal energy content of the plasma

$P_\alpha \sim \langle\sigma v\rangle$ = fusion alpha-particle self-heating

P_{aux} = auxiliary heating

$P_{rad} \sim L_z(T)$ = radiative power loss

$P_{tran} \sim U/\tau_E$ = transport power loss.

The general nature of the fusion thermal instability can be understood by assuming that a power balance is achieved for certain equilibrium values of T_0, U_0, and P_{x0} and then a small perturbation in temperature δT occurs. The linearized power balance equation is

$$dU/dt = [(\partial P_\alpha/\partial T + \partial P_{aux}/\partial T) - (\partial P_{rad}/\partial T + \partial P_{tran}/\partial T)]\delta T \ . \qquad (45)$$

If dU/dt is of the same sign as δT, the power balance is unstable, leading to a condition for stability $[(\partial P_\alpha/\partial T + \partial P_{aux}/\partial T) - (\partial P_{rad}/\partial T + \partial P_{tran}/\partial T)] \le 0$. The fusion heating term $\partial P_\alpha/\partial T > 0$ because $\langle\sigma v\rangle \sim T^2$; the auxiliary heating term may be ≤ 0 or ≥ 0 depending on the mechanism of heating. The radiation power loss term $\partial P_{rad}/\partial T \sim \partial L_z(T)/\partial T$ may be stabilizing if $\partial L_z(T)/\partial T > 0$ or destabilizing if $\partial L_z(T)/\partial T < 0$; if most of the radiation is coming from bremsstrahlung, then $\partial L_z(T)/\partial T > 0$, and the radiation term is stabilizing. The transport loss term $\sim\partial(T/\tau_E)/\partial T$ may be stabilizing or destabilizing, depending on the temperature dependence of the energy confinement time.

More detailed analyses of the thermal stability of the global electron and ion energy balances and the coupled global ion, impurity, and fusion alpha-particle balances to coupled temperature and density perturbations were developed,[1,193–199] and it was demonstrated that thermally unstable plasma equilibria could be controlled by varying the fueling or auxiliary heating rate. The use of spatially dependent radial balance equations[200–202] led to the same qualitative global thermal instability characteristics but different quantitative stability requirements.

VIII.B. Control Mechanisms

There has been substantial investigation of different mechanisms for controlling the fusion thermal instability. Modulation of auxiliary power has been well demonstrated[194,203–215] as a robust method to control fusion-driven thermal instabilities. Modulation of the fuelin g rate has also been demonstrated[194,196,199,202,208,216–219] as an effective means for controlling the fusion thermal instability. The effects of a number of other phenomena on controlling the fusion thermal instability have been examined:

1. transport losses due to toroidal magnetic field ripple via the τ_E term[220–224]
2. impurity injection[208,225]
3. the poloidal divertor[226]
4. a soft beta limit[227]
5. compressing or decompressing the plasma[228,229]

6. an ergodic magnetic limiter[230]
7. modulation of divertor pumping[208,231]
8. modification of alpha-particle transport[232,233]
9. sawtooth oscillations[234]
10. radial motion.[235]

VIII.C. Modern Control Theory

More sophisticated applications of modern control theory[236–242] to tokamak burn control have recently been introduced.

VIII.D. Applications to ITER

Several papers have been partially or totally devoted to an analysis of the stability of the proposed ITER to fusion thermal instabilities and to the control of such instabilities.[207–211,243] Following Rebhan and Veith,[243] the dynamic equations for the zero-dimensional particle balance equations for deuterium, tritium, and alpha particles, and the energy balance equation for all particles, including the electrons, are

$$\frac{d}{dt} n_D = s_D - n_D n_T \langle \sigma v \rangle (T) - \frac{n_D}{\tau_p} \tag{46}$$

and

$$\frac{d}{dt} n_T = s_T - n_D n_T \langle \sigma v \rangle (T) - \frac{n_T}{\tau_p} \tag{47}$$

and a similar equation for n_D

$$\frac{d}{dt} n_\alpha = +n_D n_T \langle \sigma v \rangle (T) - \frac{n_\alpha}{\tau_p} \tag{48}$$

and an energy balance equation

$$\frac{d}{dt}\left(\frac{3}{2} n_{tot} T\right) = n_D n_T \langle \sigma v \rangle (T) E_\alpha - \frac{3}{2} n_{tot} T/\tau_E - P_{rad} \tag{49}$$

with the assumption that the particle and energy confinement times have the same scaling $= \tau_p/\tau_E = \text{const}$ where s_D and s_T are the sources for deuterium and tritium, respectively,

$$P_{rad} = n_e n_i R_{B,1}(T) + n_e n_\alpha R_{B,2}(T) \tag{50}$$

with

$$R_{B,z_j}(T) = C_B Z_j^2 T^{1/2} g_{ff}(Z_j^2/T) \tag{51}$$

and

$$n_e = n_i + 2n_\alpha + Z n_Z \ ,$$

$$n_i = n_D + n_T \ ,$$

and

$$n_{tot} = 2n_i + 3n_\alpha + (Z+1) n_Z \ . \tag{52}$$

Cyclotron and impurity losses were neglected but could readily be included.

For the dynamic evolution of the particle and energy confinement times, three cases were considered for the confinement times: (a) τ_p and τ_E were treated as constants given by their equilibrium values, (b) a variant of the previous case, and (c) the ITER89P L-mode scaling.

The equilibrium burn conditions for a 50:50 D-T mixture and the ITER89P scaling law were determined by solving the steady-state versions of Eqs. (46) through (49). The results are shown as contours in n versus T space in Fig. 16. The constraints imposed by operational limits such as the Troyon β limit and the Greenwald density limit, as well as the performance demands such as the attainable fusion power P_{fus} or the radiation fraction $\gamma = P_{rad}/P_{\alpha x}$, are also shown. The different contours denoted by values of ρ correspond to different helium ash concentrations ranging from none ($\rho = 0$)

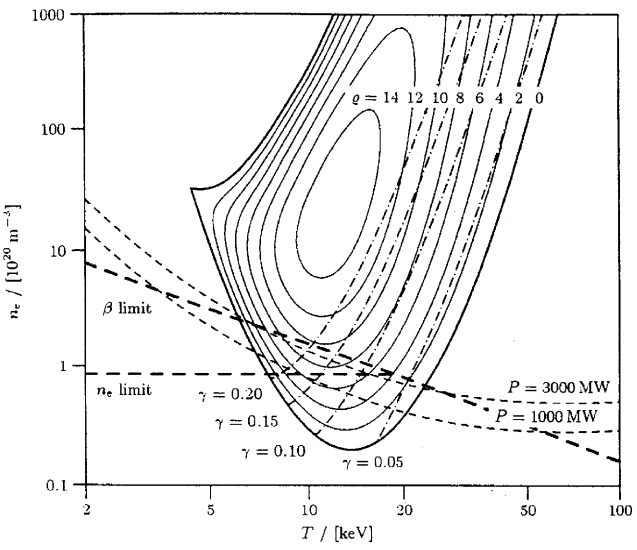

Fig. 16. Equilibrium contours with ITER-89P scaling and He concentrations varying from zero ($\rho = 0$) to the maximum for which a solution exists ($\rho = 15$—a point at center). Also shown are contours corresponding to different fusion power levels and radiation fractions (γ), as well as the beta limit with $g = 0.03$ and the Greenwald density limit contours.[243] Reprinted from *Nuclear Fusion* with permission of *Nuclear Fusion*.

to the maximum value for which ignition can be achieved ($\rho = 15$).

Using the notation $x_i = \{n_D, n_T, n_\alpha, T\}$, Eqs. (48) through (51) can be written in the form

$$\frac{dx_i}{dt} = f_i(x_1, x_2, x_3, x_4) \ , \quad i = 1,2,3,4 \ , \tag{53}$$

and the linearization around an equilibrium point x_{j0}, determined by $f_i(x_{10}, x_{20}, x_{30}, x_{40}) = 0$, results in

$$\frac{d\tilde{x}_i}{dt} = \sum_{j=1}^{4} \left. \frac{\partial f_i}{\partial x_i} \right|_{x_{j0}} \tilde{x}_j \ , \quad i = 1,2,3,4 \ , \tag{54}$$

where $\tilde{x}_j = x_j - x_{j0}$. Establishing the stability of the linearized system is then just a matter of evaluating the matrix $(a_{ij}) = (\partial f_i / \partial x_j)$ at the equilibrium point and calculating its eigenvalues.

Figure 17 shows the results of the corresponding numerical calculations in the β, T plane with the refueling rates s_D and s_T remaining at their equilibrium values. On the left branch of the ignition contours (region I), an unstable mode that is mainly a thermal fluctuation coupled to small density fluctuations is found. In a narrow region in the middle (region II), two unstable modes, which are either real or complex modes, are found. Finally, on the right branch of the ignition contours (region III), all modes were stable. The effect of the different treatments of τ_E is indicated.

Figures 16 and 17 illustrate possible thermal instabilities in the early 1998 version of the ITER design at 21-MA plasma current.[244] Control of the fusion power in the present 15-MA ITER design is considered in Ref. 245.

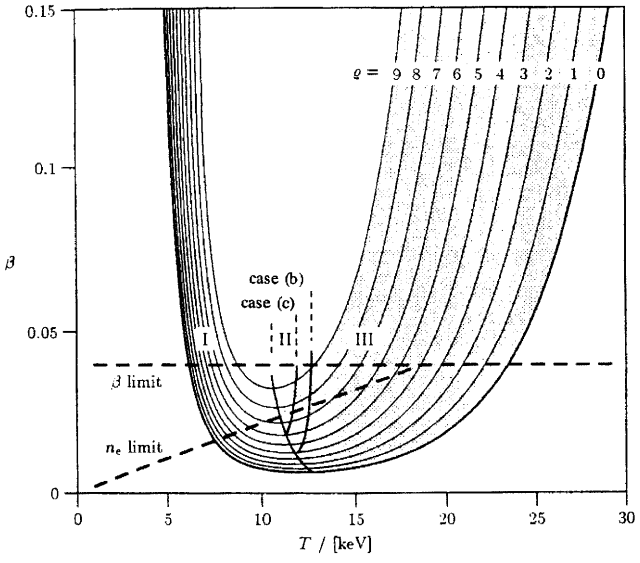

Fig. 17. Stability of burn equilibria for a 50:50 D-T mixture with ITER89P confinement scaling. Region I is unstable, region II is oscillatory and unstable, and region III is stable.[243] Reprinted from *Nuclear Fusion* with permission of *Nuclear Fusion*.

The general conclusion that can be drawn from the studies to date of fusion heating–driven thermal instabilities is that it should be possible to avoid them by the proper choice of operational parameters or to control them.

IX. DISCUSSION AND CONCLUSIONS

For more than 30 years, fusion researchers have sought to understand a variety of abrupt transitions in plasma operating conditions observed in tokamak experiments, and to anticipate others that might be present in fusion reactors, by analyzing instabilities in the coupled plasma particle, momentum, and energy balances—i.e., thermal instabilities. The strong temperature dependence, over certain temperature ranges, of the radiation cooling rate of low-Z impurities, of the atomic physics cooling and particle source rates associated with recycling and fueling neutrals, of the ion-electron recombination particle loss rate, and of the fusion alpha heating rate have all been identified as "drivers" of thermal instabilities. A strong temperature dependence of the energy transport loss rate has been identified as a driver or a stabilizer of thermal instabilities, depending on the sign of the temperature dependence. Many of these drivers of thermal instabilities are primarily edge phenomena. Such thermal instabilities have been proposed to explain many observed phenomena—detachment, divertor MARFE formation, core MARFE formation, confinement degradation, pedestal deterioration, the L-H and H-L transitions, asymmetries in the power flux to inboard and outboard divertor targets, and radiative collapse of the temperature profile leading to a density-limit disruption—and to examine the stability of future fusion reactors against power level excursions.

Because the onset of the edge-related thermal instabilities can be theoretically related to local or average densities exceeding a threshold value, density limits for the onset of these observed phenomena can be related to the onset of the respective thermal instabilities. The onset conditions are determined by a balance between destabilizing terms—the impurity and atomic physics drivers—and the stabilizing terms—conduction and convection heating due to the divergence of the passing heat flux and any local external heating that does not have an unfavorable temperature dependence (as fusion heating does). Thus, the threshold densities for the onset of thermal instabilities tend to increase with the heat flux passing through the edge and with the local edge temperature gradients and to decrease with the local impurity and neutral atom concentrations. The temperature dependence of the threshold densities is more complex because of the very different temperature dependences of the various stabilizing and destabilizing terms.

Alternative explanations have been put forward for some of the above phenomena. There would seem to be broad agreement that core MARFE formation, radiative collapse leading to density limit disruptions, and divertor MARFE formation all can be understood in terms of thermal instabilities along the lines discussed in this survey, although alternative explanations have been put forward for all of the phenomena. Detachment can be understood as surveyed in this paper, but whether detachment should be regarded as the onset of a thermal instability in the power balance, or as a limit on the density for which there exists an attached solution to the power balance, remains an open question. While the work to date makes a good case that in-out asymmetries in divertor heat fluxes can be understood as thermal instabilities, there has been relatively little such work. Similarly, the thermal instability explanations of the L-H and H-L transitions and of the observed confinement degradation, while supported by experimental comparisons, is new, and there exists a much larger body of competing explanations for these particular experimental phenomena. At this point, a relatively comprehensive body of theory exists for these "radiative edge" thermal instabilities, but more extensive testing of this theory against experiment is needed.

Looking ahead to burning plasmas, the role of the destabilizing temperature dependence of the fusion cross section is well understood, several active control mechanisms have been investigated, and the possibility of inherent stabilization via the temperature dependence of thermal transport coefficients has been identified. However, there has been little, if any, examination of instability phenomena that may arise from the interaction of fusion heating instabilities in the core plasma and radiative cooling instabilities in the plasma edge and divertor (with temperature-dependent transport coefficients in both the core and edge). The interaction of the core fusion heating instability, edge radiative instabilities (e.g., MARFEs and transport enhancing), the H-mode edge pedestal, divertor detachment and divertor MARFE instabilities, etc., is quite likely to produce new phenomena. There will surely be need for interaction among the "burn control" system for the fusion power level, the radiative power exhaust control system for the plasma edge, the divertor control systems, etc., in future burning plasma devices (e.g., ITER).

REFERENCES

1. R. G. MILLS, "The Problem of Control of Thermonuclear Reactions," LA-4250, pp. 1 B1.1–B1.5, Los Alamos National Laboratory (1969).

2. H. P. FURTH, M. N. ROSENBLUTH, and P. H. RUTHERFORD, "Thermal Equilibrium and Stability of Tokamak Discharges," *Phys. Fluids*, **13**, 3020 (1970).

3. E. P. GORBUNOV and K. A. RAZUMOVA, "Effect of a Strong Magnetic Field on the Magnetohydrodynamic Stability of a Plasma and the Confinement of Charged Particles in the Tokamak Machine," *J. Nucl. Energy C*, **6**, 515 (1964).

4. N. R. SAUTHOFF, S. VON GOELER, and W. STODIEK, "A Study of Disruptive Instabilities in the PLT Tokamak Using X-Ray Techniques," *Nucl. Fusion*, **18**, 1445 (1978).

5. J. A. WESSON et al., "Disruptions in JET," *Nucl. Fusion*, **29**, 641 (1989).

6. A. GIBSON, "Radiation Limits to Tokamak Operation," *Nucl. Fusion*, **16**, 546 (1976).

7. N. OHYABU, "Density Limit in Tokamaks," *Nucl. Fusion*, **19**, 1491 (1979).

8. C. E. T. F. ASHBY and M. H. HUGHES, "A Study of the Effect of Impurity Radiation from the Peripheral Plasmas of Tokamak Reactor," *Nucl. Fusion*, **21**, 911 (1981).

9. F. W. PERKINS and R. A. HULSE, "On the Murakami Density Limit in Tokamaks and Reversed-Field Pinches," *Phys. Fluids*, **28**, 1837 (1985).

10. W. M. STACEY, "Radial Stability of the Radiative Mantle," *Phys. Plasmas*, **3**, 1012 (1996).

11. W. M. STACEY, "Density Limits in Tokamaks," *Phys. Plasmas*, **4**, 1069 (1997).

12. M. A. MAHDAVI et al., "Stability of a Radiative Mantle in ITER," *J. Nucl. Mater.*, **241–243**, 305 (1997).

13. W. M. STACEY and T. W. PETRIE, "The Role of Thermal Instabilities in Limiting the Density in DIII-D," *Phys. Plasmas*, **7**, 4931 (2000).

14. D. P. STOTLER, "Transport Simulations of a Density Limit in Radiation-Dominated Tokamak Discharges—Profile Effects," *Phys. Fluids*, **31**, 3713 (1988).

15. M. Z. TOKAR, "Modelling of Detachment in a Limiter Tokamak as a Nonlinear Phenomenon Caused by Impurity Radiation," *Plasma Phys. Control. Fusion*, **36**, 1819 (1994).

16. R. G. KLEVA and J. F. DRAKE, "Density Limit Disruptions in Tokamaks," *Phys. Fluids B*, **3**, 372 (1991).

17. U. SAMM, "Radiation Cooling Experiments and Reactor Application," *Fusion Technol.*, **25**, 259 (1994).

18. A. POSPIESZCZYK et al., "Study of the Power Exhaust and the Role of Impurities in TEXTOR," *Phys. Plasmas*, **2**, 2272 (1995).

19. G. BECKER, "Simulation of Transport in the Ignited ITER with 1.5-D Predictive Code," *Nucl. Fusion*, **35**, 39 (1995).

20. J. MANDREKAS and W. M. STACEY, "An Impurity Seeded Radiative Mantle for ITER," *Nucl. Fusion*, **35**, 843 (1995).

21. J. MANDREKAS, W. M. STACEY, and F. A. KELLY, "Impurity Seeded Radiative Power Exhaust Solutions for ITER," *Nucl. Fusion*, **36**, 917 (1986).

22. J. MANDREKAS, W. M. STACEY, and F. A. KELLY, "Robustness of Radiative Mantle Plasma Power Exhaust Solutions for ITER," *Nucl. Fusion*, **37**, 1015 (1997).

23. G. BECKER, "Transport Simulations of ITER with Empirical Heat Diffusivity Scaling," *Nucl. Fusion*, **38**, 293 (1998).

24. M. Z. TOKAR, "Non-Linear Phenomena in Textor Plasmas Caused by Impurity Radiation," *Phys. Scripta*, **51**, 665 (1995).

25. G. FUSSMANN et al., "Impurity Accumulation in Plasma Regimes with High Energy Confinement," *J. Nucl. Mater.*, **162–164**, 14 (1989).

26. R. NEU et al., in *Proc. 22nd European Conf. Controlled Fusion Plasma Physics*, Bournemouth, United Kingdom, 1995, Vol. 19C, part I, p. 65, European Physical Society (1995).

27. V. PHILLIPS et al., in *Proc. 22nd European Conf. Controlled Fusion Plasma Physics*, Bournemouth, United Kingdom, 1995, Vol. 19C, part II, p. 321, European Physical Society (1995).

28. J. RAPP, M. Z. TOKAR, and L. KÖNEN, "Transport Studies of High-Z Elements in Neon Edge Radiation Cooled Discharges in TEXTOR-94," *Plasma Phys. Control. Fusion*, **39**, 1615 (1997).

29. J. RAPP et al., *Proc. 24th European Conf. Controlled Fusion Plasma Physics*, Berchtesgaden, Germany, 1997, Vol. 21A, part IV, p. 1745, European Physical Society (1997).

30. M. Z. TOKAR et al., "The Influence of Impurities on Limiter Tokamak Plasmas and Relevant Mechanisms," *Plasma Phys. Control. Fusion*, **37**, A241 (1995).

31. M. Z. TOKAR et al., "Nature of High-Z Impurity Accumulation in Tokamaks," *Nucl. Fusion*, **37**, 1691 (1997).

32. S. V. PUTVINSKII, Sov., "Thermal Instability in a Thermonuclear Plasma," *J. Plasma Phys.*, **14**, 754 (1988).

33. YA. KOLESNICHENKO, V. V. LUTSENKO, and S. N. REZNIK, "Stability of Thermonuclear Burn in Tokamaks with Non-Inductive Current Drive," *Nucl. Fusion*, **31**, 1479 (1991).

34. D. ANDERSON, M. LISAK, and YA. KOLESNICHENKO, "Burn Stability of Tokamak Fusion Plasmas with Synergetic Current Drive," *Plasma Phys. Control. Fusion*, **33**, 455 (1991).

35. F. ENGELMANN, "Burn Stability of Tokamak Fusion Plasmas with Synergetic Current Drive," *Plasma Phys. Control. Fusion*, **34**, 881 (1992).

36. D. R. BAKER, R. T. SNIDER, and M. NAGAMI, "Observation of Cold High-Density Plasma near the Doublet III Limiter," *Nucl. Fusion*, **22**, 807 (1982).

37. F. ALLADIO et al., "The Regime of Enhanced Particle Recycling in High Density Tokamak Discharges in the Frascati Torus," *Phys. Lett. A*, **90**, 405 (1982).

38. H. NIEDERMEYER et al., *Europhysics Conference Abstracts: 11th Conf. Controlled Fusion Plasma Physics*, Aachen, Germany (1983), 7D-1, p. 43, European Physical Society (1983).

39. S. M. KAYE et al., *Proc. 11th European Conf. Controlled Fusion Plasma Physics*, Aachen, Germany, 1983, part II, p. O-10 (1983).

40. M. Z. TOKAR, "Plasma Instability at the Edge of a Tokamak," *Sov. Phys. Dokl.*, **29**, 928 (1984).

41. M. Z. TOKAR, "Ionization Instability of the Tokamak Edge Plasma with Particle Recycling from the Wall," *Phys. Scripta*, **31**, 411 (1985).

42. V. NEDOSPASOV and M. Z. TOKAR, "Two States of the Peripheral Plasma in Tokamaks," *Sov. Phys. Dokl.*, **31**, 344 (1986).

43. B. C. LIPSCHULTZ et al., "MARFE: An Edge Plasma Phenomenon," *Nucl. Fusion*, **24**, 977 (1984).

44. R. HULSE, "Numerical Studies of Impurities in Fusion Plasmas," *Nucl. Technol. Fusion*, **3**, 259 (1983).

45. J. O'ROURKE et al., *Proc. 12th European Conf. Controlled Fusion Plasma Physics*, Budapest, Hugary, 1985, Vol. 9F, part I, p. 155 (1985).

46. J. D. STRACHAN et al., *Proc. 12th European Conf. Controlled Fusion Plasma Physics*, Budapest, Hungary, 1985, Vol. 9F, part I, p. 339 (1985).

47. H. NIEDERMEYER et al., *Proc. 12th European Conf. Controlled Fusion Plasma Physics*, Budapest, Hungary, 1985, Vol. 9F, part II, p. 43 (1985).

48. B. C. LIPSCHULTZ, "Review of MARFE Phenomena in Tokamaks," *J. Nucl. Mater.*, **145–147**, 15 (1987).

49. T. E. STRINGER, *Europhysics Conference Abstracts: 12th Conf. Controlled Fusion Plasma Physics*, Budapest, Hungary, 1985, Vol. 9F-1, p. 159, European Physical Society (1985).

50. J. NEUHAUSER, W. SCHNEIDER, and R. WUNDERLICH, "Thermal Instabilities and Poloidal Asymmetries in the Tokamak Edge Plasma," *Nucl. Fusion*, **26**, 1679 (1986).

51. J. F. DRAKE, "Marfes: Radiative Condensation in Tokamak Edge Plasma," *Phys. Fluids*, **30**, 2429 (1987).

52. E. N. PARKER, "Instability of Thermal Fields," *Astrophys. J.*, **117**, 431 (1953).

53. G. B. FIELD, "Thermal Instability," *Astrophys. J.*, **142**, 531 (1965).

54. M. A. MAHDAVI et al., *Proc. 24th European Conf. Controlled Fusion Plasma Physics*, Petit-Lancy, Switzerland, 1997.

55. S. R. CHOUDHURY and P. K. KAW, "Ionization and Edge-Density Gradient Effects on MARFE Instabilities in Tokamak Plasmas," *Phys. Fluids B*, **1**, 1646 (1989).

56. S. DESHPANDE, "A One-Dimensional Model for Radiative Thermal Equilibrium and Stability of the Tokamak Edge Plasma," *Phys. Plasmas*, **1**, 127 (1994).

57. W. ROSS, "Critique of Atomic Physics Instability Mechanisms: Ionization-Driven and Radiative Microinstabilities in the Tokamak Edge Plasma," *Phys. Plasmas*, **1**, 2630 (1994).

58. P. CHEN, B. R. SHI, and Z. D. GAO, "Multifaceted Asymmetric Radiation from the Edge: A Strong Condensation Phenomenon," *Phys. Plasmas*, **3**, 4507 (1996).

59. M. Z. TOKAR et al., "Localized Recycling as a Trigger of Marfe," *J. Nucl. Mater.*, **266–269**, 958 (1999).

60. M. Z. TOKAR et al., "Study of the Relevance of Thermal Instability Caused by Impurity Radiation to MARFE Development in a Limiter Tokamak," *Contrib. Plasma Phys.*, **42**, 290 (2002).

61. M. Z. TOKAR and F. A. KELLY, "The Role of Plasma-Wall Interactions in Thermal Instabilities at the Tokamak Edge," *Phys. Plasmas*, **10**, 4378 (2003).

62. F. A. KELLY and M. Z. TOKAR, "Theoretical Study of the Effect of the Dynamic Ergodic Divertor on MARFE Onset," *Contrib. Plasma Phys.*, **44**, 176 (2004).

63. U. SAMM et al., "MARFE Feedback Experiments on TEXTOR-94," *J. Nucl. Mater.*, **266–269**, 666 (1999).

64. J. RAPP et al., "Operational Limits Under Different Wall Conditions on TEXTOR-94," *J. Nucl. Mater.*, **290–293**, 1148 (2001).

65. W. M. STACEY, "Explanation for MARFE Formation and Subsequent Evolution in a Detached Symmetric Plasma Edge," *Phys. Plasmas*, **3**, 2673 (1996).

66. W. M. STACEY, "Thermal Stability of the Tokamak Edge Plasma," *Plasma Phys. Control. Fusion*, **39**, 1245 (1997).

67. W. M. STACEY, "Density Limits for Multifaceted Asymmetric Radiation from the Edge," *Fusion Technol.*, **36**, 38 (1999).

68. J. J. MARTINELL, "Edge Energy Balance and Temperature Scalings in a Tokamak," *Phys. Plasmas*, **1**, 937 (1994).

69. YU. L. IGITKHANOV, *Plasma Phys. Control. Fusion*, **28**, 477 (1988).

70. J. A. WESSON and T. C. HENDER, "An Extended Treatment of MARFE Stability," *Nucl. Fusion*, **33**, 1019 (1993).

71. J. KESNER and J. P. FREIDBERG, "MARFE Formation in Diverted Tokamaks," *Nucl. Fusion*, **35**, 115 (1995).

72. Y. LIANG et al., "Influence of the Dynamic Ergodic Divertor on the Density Limit in TEXTOR," *Phys. Rev. Lett.*, **94**, 105003 (2005).

73. D. E. POST, "A Survey of Recent Developments in Atomic Processes for Divertors and Edge Plasmas," *J. Nucl. Mater.*, **220–222**, 143 (1995).

74. S. I. KRASHENINNIKOV et al., "Effect of the Dynamics of the Impurity Distribution over the Ionization States on the Radiative Plasma Instabilities and Shock Wave Structure," *Contrib. Plasma Phys.*, **36**, 271 (1996).

75. C. R. McCARTHY, A. E. BOOTH, J. E. HUTCHINSON, and S. I. KRASHENINNIKOV, "Nonlinear Behavior of Radiative Modes in Noncoronal Equilibrium," *Phys. Plasmas*, **4**, 2567 (1997).

76. F. A. KELLY, W. M. STACEY, J. RAPP, and M. BRIX, "Thermal Instability Analysis of Multifaceted Asymmetric Radiation from the Edge (MARFE) in TEXTOR," *Phys. Plasmas*, **8**, 3382 (2001).

77. W. M. STACEY, "Multifaceted Asymmetric Radiation from the Edge: Impurity Density Limits in Tokamaks with Poloidal Asymmetry and Rotation," *Phys. Plasmas*, **3**, 3032 (1996).

78. W. M. STACEY, "Multifaceted Asymmetric Radiation from the Edge Suppression by External Edge Heating," *Phys. Plasmas*, **4**, 134 (1997).

79. W. M. STACEY, "Validity of the Impurity Entrainment Assumption in the Thermal Stability Analysis of Multifaceted Asymmetric Radiation from the Edge in Tokamak Plasmas," *Phys. Plasmas*, **4**, 242 (1997).

80. W. M. STACEY, "Effect of Convection on Multifaceted Asymmetric Radiation for Edge Density Limits," *Phys. Plasmas*, **7**, 3464 (2000).

81. J. M. ALLEN et al., "Studies of Diverted Plasmas and High Density Disruption in DITE," *Plasma Phys. Control. Fusion*, **28**, 101 (1986).

82. G. M. McCRACKEN et al., "A Study of Detached Plasmas in the DITE Tokamak," *J. Nucl. Mater.*, **145**, 181 (1987).

83. U. SAMM et al., "Influence of Impurity Radiation Losses on Plasma Edge Properties in TEXTOR," *J. Nucl. Mater.*, **176**, 273 (1990).

84. J. D. STRACHAN et al., "Experimental Results from Detached Plasmas in TFTR," *J. Nucl. Mater.*, **145–147**, 186 (1987).

85. F. P. BOODY et al., "Phenomenology of MARFEs in TFTR," *J. Nucl. Mater.*, **145**, 196 (1987).

86. G. WAIDMANN and G. KUANG, "Density Limits and Evolution of Disruptions in Ohmic TEXTOR Plasmas," *Nucl. Fusion*, **32**, 645 (1992).

87. J. RAPP et al., "Density Limits in TEXTOR-94 Auxiliary Heated Discharges," *Nucl. Fusion*, **39**, 765 (1999).

88. U. SAMM et al., "Plasma Edge Physics with Siliconization in TEXTOR," *J. Nucl. Mater.*, **220–222**, 25 (1995).

89. C. E. BUSH et al., "Ohmic and Neutral Beam Heated Detached Plasmas on TFTR," *J. Nucl. Mater.*, **176–177**, 792 (1990).

90. P. K. KAW, S. DESHPANDE, K. AVINASH, and S. RATH, "Asymmetric Radiative Equilibria in Tokamak Edge and the Detached Plasma Transition," *Phys. Rev. Lett.*, **65**, 2873 (1990).

91. M. Z. TOKAR, "On Threshold of Radial Detachment in Tokamaks," *Phys. Plasmas*, **7**, 2432 (2000).

92. T. W. PETRIE, A. G. KELLMAN, and M. A. MAHDAVI, "Plasma Density Limits During Ohmic L Mode and ELMing H Mode Operation in DIII-D," *Nucl. Fusion*, **33**, 929 (1993).

93. T. W. PETRIE et al., "Radiative Divertor Experiments in DIII-D with D_2 Injection," *Nucl. Fusion*, **37**, 321 (1997).

94. T. W. PETRIE et al., "Investigation of Electron Parallel Pressure Balance in the Scrapeoff Layer of Deuterium-Based Radiative Divertor Discharges in DIII-D," *J. Nucl. Mater.*, **241–243**, 639 (1997).

95. R. MAINGI et al., "Investigation of Physical Processes Limiting Plasma Density in High Confinement Mode Discharges in DIII-D," *Phys. Plasmas*, **4**, 1752 (1997).

96. W. SUTTROP et al., "Operational Limits for High Edge Density H-Mode Tokamak Operation," *J. Nucl. Mater.*, **266–269**, 118 (1999).

97. A. LOARTE et al., "Plasma Detachment in JET Mark I Divertor Experiments," *Nucl. Fusion*, **38**, 331 (1998).

98. N. HOSOGANE et al., "Radiative Divertor in JT60-U," *J. Nucl. Mater.*, **220–222**, 420 (1995).

99. B. LIPSCHULTZ et al., "Dissipative Divertor Operation in the Alcator C-Mod Tokamak," *J. Nucl. Mater.*, **220–222**, 50 (1995).

100. G. F. MATTHEWS, "Plasma Detachment from Divertor Targets and Limiters," *J. Nucl. Mater.*, **220–222**, 104 (1995).

101. J. NEUHAUSER et al., "The Compatibility of High Confinement Times and Divertor Detachment in ASDEX-Upgrade," *Plasma Phys. Control. Fusion*, **37**, A37 (1995).

102. J. A. GOETZ et al., "Comparison of Detached and Radiative Divertor Operation in Alcator C-Mod," *Phys. Plasmas*, **3**, 1908 (1996).

103. M. E. FENSTERMACHER et al., "The Two-Dimensional Structure of Radiative Divertor Plamas in the DIII-D Tokamak," *Phys. Plasmas*, **4**, 1761 (1997).

104. G. D. PORTER et al., "Simulation of Experimentally Achieved DIII-D Detached Plasmas Using the UEDGE Code," *Phys. Plasmas*, **3**, 1967 (1996).

105. H-S. BOSCH et al., "2D Modelling of the ASDEX-U Scrape-Off Layer and Divertor Plasmas," *J. Nucl. Mater.*, **220–222**, 558 (1995).

106. D. P. COSTER et al., "B2-Eirene Modeling of ASDEX Upgrade," *J. Nucl. Mater.*, **241–243**, 690 (1997).

107. A. LOARTE et al., "Comparison Between Measure Scrape-Off Layer Plasma Parameters and 2D Model Calculations for JET X-pt Discharges," *J. Nucl. Mater.*, **220–222**, 606 (1995)

108. S. TSUJU et al., "Two-Dimensional Divertor Simulation on JT-60U," *J. Nucl. Mater.*, **220–222** (1995).

109. A. HATAYAMA et al., "High Mach Flow Associated with X-Point MARFE and Plasma Detachment," *Nucl. Fusion*, **40**, 2009 (2000).

110. D. P. STOTLER et al., "Coupled Monte Carlo Neutral-Fluid Plasma Simulation of Alcator C-Mod Divertor Plasma near Detachment," *J. Nucl. Mater.*, **266–269**, 947 (1999).

111. A. LOARTE, "Understanding the Edge Physics of Divertor Experiments by Comparison of 2D Edge Calculations and Experimental Measurements," *J. Nucl. Mater.*, **241–243**, 118 (1997).

112. K. BORRASS, D. COSTER, D. REITER, and R. SCHNEIDER, "Study of Recombining Gas Targets," *J. Nucl. Mater.*, **241–243**, 250 (1997).

113. G. M. McCRACKEN et al., "Volume Recombination and Detachment in JET Divertor Plasma," *J. Nucl. Mater.*, **266–269**, 37 (1999).

114. W. M. STACEY, M. A. MAHDAVI, R. MAINGI, and T. W. PETRIE, "Multi-Faceted Asymmetric Radiation from the Edge Formation in DIII-D High-Confinement Mode Discharges with Continuous Gas Puffing," *Phys. Plasmas*, **6**, 3941 (1999).

115. W. M. STACEY, T. W. PETRIE, and A. W. LEONARD, "Thermal Instability Explanation of Similar Density Limits in Gas Fueled, DIII-D H-Mode Shots with Different Operating Conditions," *Phys. Plasmas*, **9**, 888 (2002).

116. W. M. STACEY, T. W. PETRIE, and T. H. OSBORNE, "Thermal Instability Analysis of Different Types of Density Limits in DIII-D Gas Fueled, High-Mode Discharges," *Phys. Plasmas*, **9**, 4174 (2002).

117. A. DePLOEY et al., "Marfes: A Magnetohydrodynamic Stability Study of Two-Dimensional Tokamak Equilibria," *Plasma Phys. Control. Fusion*, **39**, 423 (1997).

118. YU. IGITKHANOV and M. MIKHAILOV, "MARFE Onset Conditions and Stability," *J. Nucl. Mater.*, **266–269**, 251 (1999).

119. M. Z. TOKAR, "On the Importance of Parallel Heat Conduction and Magnetic Geometry for Multifaceted Radiation from the Edge (MARFE)," *Phys. Plasmas*, **8**, 2866 (2001).

120. KH. MOROZOV and J. HERRERA, "Radiative Instabilities in Plasmas: Impurity Motion and Recombination Effects," *Plasma Phys. Control. Fusion*, **37**, 285 (1995).

121. B. C. LIPSCHULTZ et al., "Ultrahigh Densities and Volume Recombination Inside the Separatrix of the Alcator C-Mod Tokamak," *Phys. Rev. Lett.*, **81**, 1007 (1998).

122. G. SERGIENKO et al., "Spectroscopic Studies of Stationary MARFEs in TEXTOR-94," *J. Nucl. Mater.*, **290–293**, 720 (2001).

123. S. I. KRASHENINNIKOV, B. LIPSCHULTZ, and J. L. TERRY, in *Proc. 25th Conf. Controlled Fusion Plasma Physics*, Prague, Czech Republic, 1998, p. 441, European Physical Society (1998).

124. A. N. SIMAKOV and S. I. KRASHENINNIKOV, "Ionization-Recombination Instability and Multifaceted Asymmetric Radiation from the Edge in Magnetic Fusion Devices," *Phys. Plasmas*, **7**, 950 (2000).

125. T. W. PETRIE, "DIII-D," Personal Communication (2004).

126. N. ASAKURA et al., "Field Reversal Effects on Divertor Plasmas Under Radiative and Detached Conditions in JT-60U," *Nucl. Fusion*, **36**, 795 (1996).

127. R. SINGH et al., "Short Scale Radiative Condensation Instabilities in Tokamak Edge Plasma," *Nucl. Fusion*, **32**, 379 (1992).

128. A. V. CHANKIN, "On the Poloidal Localization and Stability of Multifaceted Asymmetric Radiation from the Edge (MARFE)," *Phys. Plasmas*, **11**, 1484 (2004).

129. M. Z. TOKAR, "Non-Linear Effects in Particle and Heat Balances of Edge Plasmas," *Contrib. Plasma Phys.*, **32**, 341 (1992).

130. A. DePLOEY, M. GOOSSENS, and R. A. M. VAN DER LINDEN, "Multifaceted Asymmetric Radiation from the Edge (MARFEs): A General Magnetohydrodynamic Study in a One-Dimensional Tokamak Model," *Phys. Plasmas*, **1**, 2623 (1994).

131. H. KASTELEWICZ, R. SCHNEIDER, and J. NEUHAUSER, "Numerical Marfe Studies for Deuterium-Carbon Plasma at ASDEX Updgrade," *Plasma Phys. Control. Fusion*, **37**, 723 (1995).

132. R. ZAGORSKI et al., "Numerical Modeling of MARFE Phenomenon near the Bumper Limiter in TEXTOR-94," *Contrib. Plasma Phys.*, **40**, 405 (2000).

133. X. Q. XU et al., "Transitions of Turbulence in Plasma Density Limits," *Phys. Plasmas*, **10**, 1773 (2003).

134. T. D. ROGNLIEN, B. J. BRAAMS, and D. A. KNOLL, "Progress in Integrated @-D Models for Analysis of Scrape-Off Layer Transport Physics," *Contr. Plasma Phys.*, **36**, 105 (1996); see also T. D. ROGNLIEN, D. D. RYUTOV, N. MATTOR, and G. D. PORTER, "Two-Dimensional Electric Fields and Drifts near the Magnetic Separatrix in Divertor Tokamaks," *Phys. Plasmas*, **6**, 1851 (1999).

135. X. Q. XU, R. H. COHEN, T. D. ROGNLIEN, and J. R. MYRA, "Low-to-High Confinement Transition Simulations in Divertor Geometry," *Phys. Plasmas*, **7**, 1951 (2000).

136. B. MEERSON, N. PETVIASHVILI, and T. TAJIMA, "Multifaceted Asymmetric Radiation from the Edge of Tokamak Plasmas (MARFE): Pattern Formation Under Nonlocal Constraints," *Phys. Plasmas*, **2**, 414 (1995).

137. T. BIRK, "Thermal Condensation Modes in Weakly Ionized Hydrogen Plasmas," *Phys. Plasmas*, **7**, 3811 (2000).

138. M. Z. TOKAR, "Consideration of Multifaceted Asymmetric Radiation for the Edge (MARFE) as a Dissipative Structure," *Phys. Plasmas*, **9**, 1646 (2002).

139. C. D. C. STEELE and M. H. IBÁÑEZ S., "Nonlinear Instability of Nonhomogeneous Thermal Structures," *Phys. Plasmas*, **4**, 618 (1999).

140. C. D. C. STEELE and M. H. IBÁÑEZ S., "Nonlinear Thermal Instability in Two Dimensions," *Phys. Plasmas*, **6**, 3086 (1999).

141. K. BORRASS, "Disruptive Tokamak Density Limit as a Scrape-Off Layer/Divertor Phenomenon," *Nucl. Fusion*, **31**, 1035 (1991).

142. K. BORRASS, R. SCHNEIDER, and R. FARENGO, "A Scrape-Off Layer Based Model for Hugill-Greenwald Type Density Limits," *Nucl. Fusion*, **37**, 523 (1997).

143. P. C. STANGEBY, "Can Detached Divertor Plasmas be Explained as Self-Sustained Gas Targets?" *Nucl. Fusion*, **33**, 1695 (1993).

144. W. M. STACEY, "A Coupled Plasma-Neutrals Model for Divertor Simulations," *Phys. Plasmas*, **5**, 1015 (1998).

145. R. MAINGI et al., "Density Limit Studies on DIII-D," *J. Nucl. Mater.*, **266–269**, 598 (1999).

146. M. A. MAHDAVI et al., "Physics of Pedestal Density Profile Formation and Its Impact on H-Mode Density Limit in Burning Plasmas," *Phys. Plasmas*, **10**, 3984 (2003).

147. T. W. PETRIE et al., "Divertor Heat Flux Reduction by D2 Injection in DIII-D," *J. Nucl. Mater.*, **196–198**, 842 (1992).

148. D. H. CAPES et al., "Thermal Equilibrium in a Diverted Plasma," *Plasma Phys. Control. Fusion*, **30**, 103 (1990).

149. D. H. CAPES, PH. GHENDRIH, and A. SAMAIN, "Radiative Instability in a Diverted Plasma," *Phys. Fluids B*, **4**, 1287 (1992).

150. PH. GHENDRIH, "Bifurcation to a Marfing Divertor Plasma Governed by Charge Exchange," *Phys. Plasmas*, **1**, 1929 (1994).

151. PH. GHENDRIH et al., "Bifurcation to Divertor MARFEs on DIII-D," *J. Nucl. Mater.*, **220–222**, 305 (1995).

152. S. I. KRASHENINNIKOV, P. J. CATTO, P. HELANDER, and D. J. SIGMAR, "Thermal Bifurcation of Scrape-Off Layer Plasma and Divertor Detachment," *Phys. Plasmas*, **2**, 2717 (1995).

153. F. WISING, S. I. KRASHENINNIKOV, and D. J. SIGMAR, "Simulation of Plasma Flux Detachment in Alcator C-Mod and ITER," *J. Nucl. Mater.*, **241–243**, 273 (1997).

154. S. I. KRASHENINNIKOV et al., "Stability of the Detachment Front in a Tokamak Divertor," *J. Nucl. Mater.*, **266–269**, 251 (1999).

155. S. NAKAZAWA, N. NAKJIMA, M. OKAMOTO, and N. OHYABU, "One-Dimensional Simulation on Stability of Detached Plasma in a Tokamak Divertor," *Plasma Phys. Control. Fusion*, **42**, 401 (2000).

156. W. M. STACEY, "Detachment and Divertor Temperature and Density Redistribution," *Phys. Plasmas*, **8**, 525 (2001).

157. S. I. KRASHENINNIKOV, "Two-Dimensional Effects in Plasma Radiation Fronts and Radiation Front Jumps in Tokamak Divertor Plasmas," *Phys. Plasmas*, **4**, 3741 (1997).

158. S. I. KRASHENINNIKOV, A. A. BATISCHEVA, and A. N. SIMAKOV, "Radiation Fronts in Tokamak Divertor Plasmas," *Phys. Plasmas*, **5**, 2297 (1998).

159. D. N. HILL et al., in *Proc. 13th Int. Conf. Plasma Physics Controlled Nuclear Fusion Research*, Washington, D.C., 1990, Vol. 3, p. 487, International Atomic Energy Agency (1991).

160. G. F. MATTHEWS, "Plasma Detachment from Divertor Targets and Limiters," *J. Nucl. Mater.*, **220–222**, 104 (1995).

161. G. M. STAEBLER, "The Critical Point for the Onset of Divertor Flux Asymmetry in Tokamaks," *Nucl. Fusion*, **36**, 1437 (1996).

162. P. J. HARBOUR et al., "The X-Point Scrape-Off Plasma in Jet with L- and H-Modes," *J. Nucl. Mater.*, **162–164**, 236 (1989).

163. N. HAYASHI, T. TAKIZUKA, A. HATAYAMA, and M. OGASAWARA, "Onset Condition of Thermoelectric Instability in Divertor Tokamaks," *Nucl. Fusion*, **38**, 1695 (1998).

164. N. HAYASHI, T. TAKIZUKA, and K. SHIMIZU, "Thermoelectric Instability in Externally Induced Asymmetric Divertor Plasmas," *Contrib. Plasmas Phys.*, **40**, 387 (2000).

165. Y. SHIBATA, A. HATAYAMA, N. HAYASHI, and M. OGASAWARA, "Numerical Simulation of Nonlinear Evolution Thermoelectric Instability in Diverted Plasmas," *Contrib. Plasma Phys.*, **40**, 393 (2000).

166. W. M. STACEY, "Thermal Instabilities in the Edge Transport Barrier," *Phys. Plasmas*, **6**, 2452 (1999).

167. W. M. STACEY, "Spontaneous Edge Transport Barrier Formation due to Suppression of Edge Thermal Instabilities as a Low-High Trigger Mechanism in Tokamaks," *Phys. Plasmas*, **9**, 3082 (2002).

168. W. M. STACEY and T. W. PETRIE, "Testing of an Edge Thermal Instability Stabilization Model for the High-to-Low Mode Power Threshold," *Phys. Plasmas*, **10**, 3949 (2003).

169. W. M. STACEY, "Testing of an Edge Thermal Instability Stabilization Model for the Low-to-High Mode Power Threshold," *Phys. Plasmas*, **11**, 686 (2004).

170. R. MAINGI et al., "Investigation of Physical Processes Limiting Plasma Density in High Confinement Mode Discharges in DIII-D" *Phys. Plasmas*, **4**, 1752 (1997).

171. W. SUTTROP et al., "Operational Limits for High Edge Density H-Mode Tokamak Operation," *J. Nucl. Mater.*, **266–269**, 118 (1999).

172. M. GREENWALD, "Density Limits in Toroidal Plasmas," *Plasma Phys. Control. Fusion*, **44**, R27 (2002).

173. W. M. STACEY, "Edge Pedestal Deterioration in Tokamak High-Mode Discharges," *Phys. Plasmas*, **8**, 5199 (2001).

174. W. M. STACEY, "Prediction of Density Limits in Tokamaks," *Phys. Plasmas*, **9**, 2692 (2002).

175. J. W. CONNOR and H. R. WILSON, "A Review of Theories of the L-H Transition," *Plasma Phys. Control. Fusion*, **42**, R1 (2000).

176. B. N. ROGERS, J. F. DRAKE, and A. ZEILER, "Phase Space of Tokamak Edge Turbulence, the L-H Transition, and the Formation of the Edge Pedestal," *Phys. Rev. Lett.*, **81**, 4396 (1998).

177. P. N. GUZDAR, R. G. KLEVA, A. DAS, and P. K. KAW, "Zonal Flow and Zonal Magnetic Field Generation by Finite β Drift Waves: A Theory for Low to High Transitions in Tokamaks," *Phys. Rev. Lett.*, **87**, 015001 (2001).

178. P. N. GUZDAR, R. G. KLEVA, R. J. GROEBNER, and P. GOHIL, "Low to High Confinement Transition Theory of Finite-Beta Drift-Wave Driven Shear Flow and Its Comparison with Data from DIII-D," *Phys. Plasmas*, **11**, 1109 (2004).

179. M. Z. TOKAR, F. A. KELLY, and X. LOOZEN, "Role of Thermal Instabilities and Anomalous Transport in Threshold Detachment and Multifaceted Asymmetric Radiation from the Edge (MARFE)," *Phys. Plasmas*, **12**, 052510 (2005).

180. M. Z. TOKAR, "Synergy of Anomalous Transport and Radiation in the Density Limit," *Phys. Rev. Lett.*, **91**, 095001 (2003).

181. M. MURAKAMI, J. D. CALLEN, and L. A. BERRY, "Some Observations on Maximum Densities in Tokamak Experiments," *Nucl. Fusion*, **16**, 347 (1976).

182. P. E. STOTT et al., *Proc. 8th European Conf. Controlled Fusion Plasma Physics*, Prague, Czech Republic, 1979, Vol. 1, p. 151, European Physical Society (1979).

183. M. GREENWALD et al., "A New Look at Density Limits in Tokamaks," *Nucl. Fusion*, **28**, 2199 (1988).

184. M. A. MAHDAVI et al., *Nucl Fusion*, **42**, 52 (2002).

185. J. STOBER et al., "Behaviour of Density Profiles of H-Mode Discharges in ASDEX Upgrade," *Plasma Phys. Control. Fusion*, **44**, A159 (2002).

186. M. VALOVIC et al., "Long Timescale Density Peaking in JET," *Plasma Phys. Control. Fusion*, **44**, 1911 (2002).

187. P. C. DE VRIES, J. RAPP, F. C. SCHÜLLER, and M. Z. TOKAR, "Influence of Recycling on the Density Limit in TEXTOR-94," *Phys. Rev. Lett.*, **80**, 3519 (1998).

188. M. GREENWALD, "Density Limits in Toroidal Plasmas," *Plasma Phys. Control. Fusion*, **44**, R27 (2002).

189. J. A. WESSON, *Tokamaks*, 2nd ed., Clarendon Press, Oxford (1997).

190. F. A. KELLY, W. M. STACEY, and J. RAPP, "Parametric Dependence of Density Limits in TEXTOR: Comparison of Thermal Instability Theory with Experiment," *Phys. Plasmas*, **8**, 4879 (2001).

191. A. LOARTE et al., "Plasma Detachment in JET Mark-I Divertor Experiments," *Nucl. Fusion*, **38**, 331 (1998).

192. W. M. STACEY, Z. W. FRIIS, T. W. PETRIE, and A. W. LEONARD, "Investigation of the Cause of the H-L Confinement Transition Following MARFE Formation in DIII-D," *Phys. Plasmas*, **12**, 072518 (2005).

193. M. OHTA, H. YAMATO, and S. MORI, "Thermal Instability and Control of Fusion Reactor," *Proc. Conf. Plasma Physics Controlled Thermonuclear Fusion Research*, 1971, International Atomic Energy Agency (1971).

194. C. POWELL and O. J. HAHN, "Energy-Balance Instabilities in Fusion Plasmas," *Nucl. Fusion*, **12**, 667 (1972).

195. W. M. STACEY, "Operating Regimes of Controlled Thermonuclear Reactors and Stability Against Fundamental Mode Excursions in Particle Densities and Temperatures," *Nucl. Fusion*, **13**, 843 (1973).

196. M. OHTA, H. YAMATO, and S. MORI, "Thermal Instability and Control of Inhomogeneous Plasma in a D-T Fusion Reactor," *J. Nucl. Sci. Technol.*, **10**, 353 (1973).

197. YA. I. KOLESNICHENKO and S. N. REZNIK, "Energy Balance Instability of a Plasma in the Thermonuclear Reactor," *Nucl. Fusion*, **13**, 167 (1973).

198. T. FUJISAWA, "Effect of Injection Fuel Energy on Fusion Reactor Stability and Feedback Control," *Nucl. Fusion*, **14**, 173 (1974).

199. W. M. STACEY, "Temperature-Density Stability in Tokamak Reactors Operating on the D-T Cycle," *Nucl. Fusion*, **15**, 63 (1975).

200. J. KESNER and R. W. CONN, "Space-Dependent Effects on the Lawson and Ignition Conditions and Thermal Equilibria in Tokamaks," *Nucl. Fusion*, **16**, 397 (1976).

201. W. A. HOULBERG and R. W. CONN, "Space-Dependent Thermal Stability of Reacting Tokamak Plasmas," *Nucl. Fusion*, **19**, 81 (1979).

202. V. FUCHS, L. HARTEN, and A. BERS, "On Tokamak Ignition Equilibria and Thermal Stability," *Nucl. Fusion*, **20**, 630 (1980).

203. L. BROMBERG, J. L. FISCHER, and D. R. COHN, "Active Burn Control of Nearly Ignited Plasmas," *Nucl. Fusion*, **20**, 203 (1980).

204. L. HARTEN, V. FUCHS, and A. BERS, "Creating Stable Tokamak Reactor Equilibria by Supplemental Heating," *Nucl. Fusion*, **20**, 833 (1980).

205. I. MAYA and H. D. CAMPBELL, "Control for Fusion Thermal Stability," *Nucl. Technol. Fusion*, **4**, 135 (1983).

206. E. A. CHANIOTAKIS, J. P. FREIDBERG, and D. R. COHN, "CIT Burn Control Using Auxiliary Power Modulation," *Proc. 13th Symp. Fusion Engineering*, p. 400, Institute of Electrical and Electronics Engineers (1990).

207. S. W. HANEY, L. J. PERKINS, J. MANDREKAS, and W. M. STACEY, "Active Control of Thermonuclear Burn Conditions for the International Thermonuclear Experimental Reactor (ITER)," *Fusion Technol.*, **18**, 609 (1990).

208. J. MANDREKAS and W. M. STACEY, "Evaluation of Different Control Methods for the Thermal Stability of the International Thermonuclear Reactor (ITER)," *Fusion Technol.*, **19**, 57 (1991).

209. J. MANDREKAS, W. M. STACEY, and H. HE, "1-1/2D Transport Studies of ITER Burn Control Scenarios," *Fusion Technol.*, **19**, 1307 (1991).

210. H. BURBAUMER, G. KAMELANDER, D. J. SIGMAR, and F. WISING, "Helium Oscillations in Burning Tokamaks," *Fusion Sci. Technol.*, **35**, 280 (1999).

211. H. BURBAUMER and G. KAMELANDER, "Study on Kinetic Control Mechanisms for ITER-Like Plasmas," *Fusion Sci. Technol.*, **37**, 131 (2000).

212. YA. I. KOLESNICHENKO, V. V. LUTSENKO, and S. N. REZNIK, "Investigation of Ignition Conditions and Thermally Unstable Burn in Plasma," *Fusion Technol.*, **25**, 84 (1994).

213. YA. I. KOLESNICHENKO, V. V. LUTSENKO, and S. N. REZNIK, "Stability of Thermonuclear Burn in Tokamaks with Non-Inductive Current Drive," *Nucl. Fusion*, **31**, 1479 (1991).

214. D. ANDERSON et al., "Maximum Q in Feedback Controlled Subignited Tokamak Fusion Plasmas," *Nucl. Fusion*, **31**, 1527 (1991).

215. E. A. CHANIOTAKIS and D. J. SIGMAR, "Time-Dependent Effects of Fusion Reactivity Enhancement due to Minority Heating in D-^{3}He Tokamak Plasmas," *Nucl. Fusion*, **33**, 849 (1993).

216. C. E. T. F. ASHBY and M. H. HUGHES, "Dynamic Burn Control of a Tokamak Reactor by Fuel Injection," *Nucl. Fusion*, **20**, 451 (1980).

217. K. MAKI, "Burn Control by Hydrogen Feeding for Self-Sustained Plasma in Tokamak Fusion Reactors," *Fusion Technol.*, **10**, 70 (1986).

218. W. HUI, B. A. BAMIEH, and G. H. MILEY, "Robust Burn Control of a Fusion Reactor by Modulation of the Refueling Rate," *Fusion Technol.*, **25**, 318 (1994).

219. J-F. WANG, T. AMANO, Y. OGAWA, and N. INOUE, "Similation of Burning Plasma Dynamics in ITER," *Fusion Sci. Technol.*, **32**, 590 (1997).

220. T. W. PETRIE and J. M. RAWLS, "Burn Control Resulting from Toroidal Field Ripple," *Nucl. Fusion*, **20**, 419 (1980).

221. T. W. PETRIE and J. M. RAWLS, "Burn Control via Regulated Ripple Applied to Reactor-Grade Plasmas," *Nucl. Fusion*, **20**, 1461 (1980).

222. L. BROMBERG and D. R. COHN, "Passive Thermal Stability Control in Ignited Tokamak by Ripple Transport and Radial Motion," *Nucl. Fusion*, **21**, 110 (1981).

223. K. BORRASS and M. SOELL, "Burn Stabilization via Feedback Ripple Regulation in an Ignited Tokamak," *Proc. 13th Symp. Fusion Technology*, p. 497 (1984).

224. K. TANI, M. AZUMI, and T. TAKIZUKA, "Passive Burn Control in a Tokamak Plasma Using Toroidal Field Ripple," *Fusion Technol.*, **18**, 625 (1990).

225. C. L. VOLD, T.-K. MAU, and R. W. CONN, "Tokamak Power Reactor Ignition and Time-Dependent Fractional Power Operation," *Fusion Technol.*, **12**, 197 (1987).

226. K. SEN, M. LISAK, and D. ANDERSON, "Feedback Control of the Thermonuclear Thermal Instability with a Poloidal Divertor Suppressor," *Nucl. Fusion*, **31**, 2392 (1991).

227. K. BORRASS, "Burn Temperature Control and Stabilization of Thermal Runaway," *Phys. Scripta*, **T16**, 107 (1987).

228. M. OKAMOTO and M. OHNISHI, "Zero-Dimensional Analysis of Burnup Control with Compression-Decompression," *J. Nucl. Sci. Technol.*, **20**, 89 (1983).

229. M. OHNISHI, A. SAIKI, and M. OKAMOTO, "Space-Dependent Analysis of Feedback Control to Suppress Thermal Runaway by Compression-Decompression," *Nucl. Technol. Fusion*, **5**, 326 (1984).

230. W. FENEBERG and G. H. WOLF, "A Helical Magnetic Limiter for Boundary Layer Control in Large Tokamaks," *Nucl. Fusion*, **21**, 669 (1981).

231. R. W. CONN, "Pumped Divertors and Limiters for Tokamaks," *Fusion Eng. Des.*, **14**, 81 (1991).

232. G. H. MILEY, S. C. HU, and V. VARADARAJAN, "Epithermal and Thermal Alpha-Particle Transport and Control," *Fusion Technol.*, **18**, 633 (1990).

233. C. S. CHANG et al., "Control of Alpha-Particle Transport by Ion Cyclotron Resonance Heating," *Fusion Technol.*, **18**, 618 (1990).

234. E. A. CHANIOTAKIS, L. BROMBER, and D. R. COHN, "Sawteeth Effects on Burn Control," PFC/JA-90-38, Massachusetts Institute of Technology (1990).

235. T. ODA et al., "Analysis of Burn Stabilization of Ignited D-T Tokamak Plasmas Allowing for Radial Motion," *Fusion Technol.*, **23**, 267 (1993).

236. A. SESTERO et al., "Preliminary Investigation of Burn Control in Experimental Tokamak Reactors," *Il Nuovo Cimento*, **62B**, 283 (1981).

237. G. C. SAGER, G. H. MILEY, and I. MAYA, "Optimal Control Theory Applied to Fusion Plasma Thermal Stabilization," *Fusion Technol.*, **8**, 1795 (1985).

238. C. E. KESSEL, M. A. FIRESTONE, and R. W. CONN, "Linear Optimal Control of Tokamak Fusion Devices," *Fusion Technol.*, **17**, 391 (1990).

239. G. H. MILEY and V. VARADARAJAN, "On Self-Tuning Control of Tokamak Thermokinetics," *Fusion Technol.*, **22**, 425 (1992).

240. D. ANDERSON et al., "Studies of Fusion Burn Control," *Fusion Technol.*, **23**, 5 (1993).

241. M. A. FIRESTONE, J. W. MORROW-JONES, and T. K. MAU, "Comprehensive Feedback Control of a Tokamak Fusion Reactor," *Fusion Sci. Technol.*, **32**, 390 (1997).

242. E. SCHUSTER, M. KRSTIC, and G. TYNAN, "Burn Control in Fusion Reactors via Nonlinear Stabilization Techniques," *Fusion Sci. Technol.*, **43**, 18 (2003).

243. E. REBHAN and U. VIETH, "Burn Stability and a Safe Operating Regime of a Tokamak Reactor with ITER Scaling," *Nucl. Fusion*, **37**, 251 (1996).

244. "Technical Basis for ITER Final Design Report, Cost Survey and Safety Analysis (FDR)," IAEA, Vienna, 1998, ITER EDA Documentation Series No. 16.

245. "Plant Description Document, Section 3.7.4.2.2, 'Kinetic Control in the Reference Inductive Scenario,'" ITER Technical Basis, ITER EDA Documentation Series No. 24, International Atomic Energy Agency (2002).